Insights into the structure and dynamics of the upper mantle beneath Bass Strait, southeast Australia, using shear wave splitting

M. Bello[*1,2], D.G. Cornwell[1], N. Rawlinson[3] and A. M. Reading[4]

[1]School of Geosciences, University of Aberdeen, Aberdeen, UK
[2]Department of Physics, Abubakar Tafawa Balewa University, Bauchi, Nigeria
[3]Department of Earth Sciences-Bullard Labs, University of Cambridge, Cambridge, UK
[4]School of Natural Sciences (Physics), University of Tasmania, Tasmania, Australia

We investigate the structure of the upper mantle using teleseismic shear wave splitting measurements obtained at 32 broadband seismic stations located in Bass Strait and the surrounding region of southeast Australia. Our dataset includes ~366 individual splitting measurements from SKS and SKKS phases. The pattern of seismic anisotropy from shear wave splitting analysis beneath the study area is complex and does not always correlate with magnetic lineaments or current N-S absolute plate motion. In the eastern Lachlan Fold Belt, fast shear waves are polarized parallel to the structural trend (~N25E). Further south, fast shear wave polarization directions trend on average N25-75E from the Western Tasmania Terrane through Bass Strait to southern Victoria, which is consistent with the presence of an exotic Precambrian microcontinent in this region as previously postulated. Stations located on and around the Neogene-Quaternary Newer Volcanics Province in southern Victoria display sizeable delay times (~2.7 s). These values are among the largest in the world and hence require either an unusually large intrinsic anisotropy frozen within the lithosphere, or a contribution from both the lithospheric and asthenospheric mantle. In the Eastern Tasmania Terrane, nearly all observed fast directions are approximately NW-SE. Although part of our data set strongly favours anisotropy originating from "fabric" frozen in the lithospheric mantle, a contribution from the asthenospheric flow related to the present day plate motion is also required to explain the observed splitting parameters. We suggest that deviation of asthenospheric mantle flow around lithospheric roots could be occurring, and so variations in anisotropy related to mantle flow may be expected. Alternatively, the pattern of fast polarisation orientations observed around Bass Strait may be consistent with radial mantle flow associated with a plume linked to the recently discovered Cosgrove volcanic track. However, it is difficult to characterise the relative contributions to the observed splitting from the lithospheric vs. asthenospheric upper mantle due to poor backazimuthal coverage of the data.

KEY WORDS: mantle anisotropy, lithosphere, asthenosphere, shear-wave splitting, SKS/SKKS phases, southeast Australia

1. Introduction

The tectonic evolution of southeast Australia's Palaeozoic orogens (part of the eastern Australian Tasmanides) is yet to be fully understood, with most of the proposed models not in agreement with regard to the presence of entrained Precambrian continental fragments (Glen, 2005; Cayley et al., 2002; Cayley, 2011, Moresi et al., 2014; Pilia et al., 2015a; Pilia et al., 2015b; Pilia et al., 2016), geometry and number of subduction zones involved in the accretionary process (Gray and Foster, 2004; Fergusson et al., 2009; Fergusson, 2014; Glen, 2014) and age and extent of metamorphism of the various tectonic blocks that form the orogens (Glen, 2005; Moore et al., 2013, Moore et al., 2015). Despite the lack of consensus, there appears little doubt that a complex sequence of events was required to build the Tasmanides, and the deformation processes involved would likely leave a clear signature of elastic wave anisotropy frozen into the lithosphere. Shear wave splitting measurements can be used to probe patterns of deformation at depth because it is an unambiguous indicator of seismic anisotropy and hence an essential tool in understanding the structure and dynamics of the Earth's deep interior (e.g. Vinnik et al., 1984; Silver and Chan, 1988; Long and Silver, 2009; Long and Becker, 2010).

In the upper mantle, seismic anisotropy results mainly from crystallographic or lattice preferred orientation (LPO) of intrinsically anisotropic mineral, primarily olivine. This is caused by deformation-induced alignment of the anisotropic minerals in the asthenosphere or past deformation of the lithosphere (e.g. Nicolas and Christensen, 1987; Silver and Chan, 1988; Zhang and Karato, 1995; Long and Becker, 2010; Mainprice et al., 2000). In addition to this, a contribution to anisotropy from shape-preferred orientation (SPO) might be present if materials with elastically distinct properties, such as melt lenses or fluid-filled microcracks, align preferentially (e.g. Silver, 1996; Silver and Chan, 1988). Some studies suggest that the alignment of fluid-filled microcracks in response to an applied stress field is a dominant cause of anisotropy in the crust (e.g. Crampin, 1987; Babuska and Cara, 1991; Crampin 1994). However, the tectonic fabric of continental regions that are subjected to strong deformation leads to lineations, foliations and other structures that develop in response to tectonic forces, and may be preserved in the crust as strain-induced mineral alignment (LPO or SPO).

When a seismic shear wave passes through an anisotropic medium, it splits into two orthogonal quasi-shear waves, one travelling faster than the other with a time lag (δt) which is observed between the "fast" and "slow" polarised shear waves when they arrive at the receiver (e.g. Silver, 1996). One of the two waves is also orientated parallel to the direction (φ) of the anisotropy, and the other is orientated perpendicular. The size of the time lag depends on the thickness of the anisotropic layer and/or the intensity of anisotropy. The time lag between the fast and slow components results in non-zero energy on the tangential-component seismogram and an elliptical particle motion. The fast-polarization orientation (φ) and time delay (δt) parameters provide simple measurements that characterize the seismic anisotropy of the medium (e.g. Silver and Chan, 1991).

The splitting parameters can be related to preserved/fossil anisotropy frozen in the lithosphere (e.g. Vauchez and Nicolas, 1991; Bastow et al., 2007), present-day sub-lithospheric flow which is principally controlled by plate motion (e.g. Vinnik et al., 1992; Fouch et al., 2000; Sleep et al., 2002), the preferential orientation of fluid or melt bodies (e.g. Blackman and Kendall, 1997), or combinations of these factors. Seismic arrivals such as SKS, PKS, and SKKS are the most suitable phases for shear wave splitting studies of the lithosphere beneath a seismic station because they involve P-to-S conversions at the core-mantle boundary. Hence, no source side anisotropy is preserved, and these phases are horizontally polarized on exiting the core-mantle boundary (e.g. Savage, 1999). The near-vertical incidence of the arrivals also results in good lateral resolution of <50 km if a dense array of seismometers is deployed (Savage, 1999).

The aim of this study is to use seismic anisotropy derived from shear wave splitting to provide insights into the lithospheric structure and possible mechanical coupling between the crust and the upper mantle beneath Bass Strait and adjoining landmasses. Data in this case is supplied by temporary and permanent arrays of broadband seismometers that span southeastern New South Wales, southern Victoria, Bass Strait and Tasmania. The study also aims to provide insight into the tectonic relationship between different tectonic blocks in the southern part of the Tasmanides.

2. Tectonic setting

At the onset of the Phanerozoic, the Australian continent witnessed a new phase of tectonic evolution dominated by subduction related accretion, which added nearly one third of the present day continental lithosphere to the eastern margin (Betts et al., 2002). The so-called Tasman Orogen or “Tasmanides” are a series of orogenic belts that have developed along the margin of eastern Australia from the Cambrian to the Triassic (Foster and Gray, 2000; Glen, 2005). These orogenic belts have an approximate NE-SW dominant structural trend and comprise the Delamerian, Lachlan, Thomson and New England Orogens (Fig. 1).

On mainland Australia, the oldest orogeny in the Tasmanides is the Delamerian Orogeny (Fig. 1). It began during the Middle Cambrian with convergence along the proto-Pacific margin of East Gondwana and culminated in a foreland style fold and thrust belt which featured high-temperature, low-pressure metamorphism associated with intrusive magmatism (Betts et al., 2002). A number of studies (e.g. Reed et al., 2002; Crawford et al., 2003) suggest that the Delamerian Orogen extends southwards from mainland Australia into western Tasmania, where it is referred to as the Tyennan Orogen. This connection is reinforced by several studies which examined the age and geochemistry of various igneous rocks in both regions, and found strong similarities (e.g. Direen and Crawford, 2003).

Adjoining the Delamerian Orogen to the east is the Lachlan Orogen whose evolution is thought to have begun in the Late Cambrian and was largely complete by the Middle to Late Devonian. The Lachlan Orogen is well known for its complex tectonic history that includes several orogenic episodes that are recorded in the rock record as a series of distinct deformational events (Gray and Foster, 2004; Glen, 2005). Previous studies (e.g. Gray and Foster, 2004) have argued for a tectonic model that involved interaction of oceanic microplates, a volcanic arc, multiple turbidite-dominated thrust systems and three major subduction zones within the Lachlan Orogen. Each of the subduction zones is associated with accretion of discrete terrains, namely the Stawell-Bendigo zones of western Victoria, the Tabbarebera zone of eastern Victoria and the Narooma accretionary complex along the east coast (Fig. 1). The evolution of the Lachlan Orogen is yet to be fully understood because of the complexity of the surface geology, the limited exposure due to the presence of Mesozoic and Cenozoic sedimentary basins and Quaternary volcanics which obscure a large proportion of the Palaeozoic terrane, and a limited knowledge of the deep structure and composition of the lithosphere.

The relationship between the Lachlan Orogen and Thomson Orogen, which lies to its North, has traditionally been difficult to determine largely because of extensive sedimentary cover from the Mesozoic Murray and Eromanga basins (Fig. 1)(Glen et al., 2013; Burton and

Trigg, 2014; Glen et al., 2014). However, recent geophysical and geochemical studies (Siegel et al., 2018; Spampinato et al., 2015) have suggested that the Thompson Orogen is floored with Precambrian continental crust, which is in contrast to the Palaeozoic oceanic substrate of the Lachlan Orogen. To the northeast of the Lachlan Orogen is the New England Orogen, which formed between the Late Devonian and Triassic and is the youngest fold belt in the Tasmanides. The New England Orogen formed as an east facing convergent margin Orogen (Glen, 2005; Rosenbaum et al., 2012) and although there is some evidence of a shared Cambrian history between the New England and Lachlan Orogens (Glen, 2013), this relationship is obscured by the presence of post emplacement sedimentary cover of the Permian to Triassic Sydney Basin.

Significant tectonic events that have shaped southeast Australia subsequent to the formation of the Tasmanides include the break up of Australia and Antarctica, and the opening of the Tasman Sea and Bass Strait around 80-90 Ma (Gaina et al., 1998). These events resulted in lithospheric thinning towards the passive margin and failed rifting in Bass Strait led to the formation of three intracratonic rift basins (Bass, Gippsland and Otway). These basins largely accommodate Cretaceous to Quaternary sediments (Lister et al., 1991; van der Beek et al., 1999).

In a recent study, it was shown that the Cosgrove volcanic track traversed almost the entire eastern seaboard of Australia (Davies et al., 2015), with its last known eruptions likely associated with the Quaternary Newer Volcanics province in western Victoria between ~4.5 Ma and 5 kyr ago (Rawlinson et al., 2017). The current location of the underlying plume – if it still exists – is roughly beneath the centre of Bass Strait (Davies et al., 2015), where a regional surface wave tomography study indicates the presence of a low velocity zone to depths of ~150 km (Fishwick and Rawlinson, 2012).

South of Bass Strait, Tasmania largely comprised what is now referred to as the West Tasmania Terrane in the Early to Middle Phanerozoic (Fig. 1)(Black et al., 2004). The evolution of this region began as long ago as 800–750 Ma (Turner et al., 1998), with pervasive granite emplacement on King Island and deposition of thick turbidite sediments in NW Tasmania. The major event that shaped western Tasmania was the Middle to Late

Cambrian Tyennan Orogeny, which was a period of significant deformation (Elliot et al., 1993). Several models have been proposed to explain the origin of the Tyennan Orogeny, which range from westerly subduction to easterly subduction to even a purely extensional regime in which the felsic Mount Read Volcanic arc formed as a result of rifting (Corbett et al., 1972). More recent models suggest that an east–facing Tasmanian passive margin collided with an oceanic arc in the Early to Middle Cambrian, resulting in obduction of mafic-ultramafic complexes across much of Tasmania (Berry and Crawford, 1988; Crawford and Berry, 1992; Turner et al., 1998). In a possible second stage of the obduction process, fault bounded Proterozoic units displaying anomalous high-grade metamorphism are also thought to have been emplaced (Berry, 1995; Maffre et al., 2000; Holm and Berry, 2002; Berry et al., 2007).

On the other hand, the East Tasmania Terrane (Fig. 1) contains no evidence of the Tyennan Orogeny or Proterozoic outcrop, and it is widely thought that the two terranes were sutured together during the Middle Devonian Tabberabberan Orogeny (Elliot et al., 1993). Differences in stratigraphy across the so-called Tamar Fracture System in northern Tasmania (Fig. 1) motivated several workers to suggest that the fracture zone represents the crustal-scale suture between the East and West Tasmania terranes (Williams, 1989). The stratigraphy exhibits Proterozoic sedimentary and Palaeozoic volcanic and sedimentary successions in the west, while a thick sequence of Lower to Middle Palaeozoic turbidites lie to the east (Reed, 2001). However, south of the Tamar Valley, widespread late Carboniferous sedimentary deposits and Jurassic dolerite sheets conceal any evidence of a crustal scale suture zone. In addition, potential field data (Leaman, 1994) do not support the existence of a major terrane boundary beneath the inferred Tamar Fracture System.

In an effort to link Tasmania and mainland Australia many models have been proposed. Although these models are often in conflict, one model that has recently gained widespread support is the Selwyn Block model of Cayley et al. (2002). Using evidence from potential field and outcrop data, Cayley et al. (2002) suggested that a Precambrian fragment of continental crust is embedded within the Tasmanides, which they termed the “Selwyn Block”. The western part of Bass Strait features strong magnetic lineaments that can be traced without major disruption from northwestern Tasmania to Victoria, which is seen as one of the primary pieces of supporting evidence for its presence. In a subsequent study, Cayley (2011) proposed a new tectonic model of southeast Australia, which involves a Proterozoic exotic microcontinent termed “VanDieland”. The microcontinent VanDieland comprises the Selwyn Block, West Tasmania Terrane and the surrounding western region of Bass Strait. This fragment, postulated to be of Rodinia origin, was embedded in a convergent accretionary margin during proto-Pacific subduction along eastern Australia. In a more recent paper, Moresi et al. (2014) suggested that the entrained microcontinent caused the formation of a large orocline that underlies the Lachlan Orogen. This occurs as a result of a complex sequence of processes including differential roll back and southward transfer of material through an extensive continental transform fault. This scenario is consistent with the model of Cayley et al. (2011).

3. Previous geophysical studies

In addition to studies which focus on geological similarities, potential field data and geodynamic modelling, other geophysical observations have been used to help discriminate between the different tectonic models that have been proposed. For example, several seismic tomography models for southeast Australia that have recently been published provide an unprecedented level of detail on crust and upper mantle structure beneath the region (e.g., Graeber et al., 2002; Rawlinson et al., 2006; Rawlinson and Urvoy 2006; Rawlinson and Kennett, 2008; Rawlinson and Fishwick, 2011; Rawlinson et al., 2015; Pilia et al., 2015a; Pilia et al., 2015b; Pilia et al., 2016; Rawlinson et al., 2016). In particular, Pilia et al., (2015a) used ambient noise tomography to image several striking structural features in the mid-lower crust beneath southeast Australia, including a NW-SE high velocity anomaly that is interpreted to be the Proterozoic connection between north-western Tasmania and south-central Victoria. This model also reveals three pronounced north-south high velocity belts that appear to span Bass Strait with little evidence of interruption from more recent tectonic events.

Studies carried out by Debayle and Kennett (1998), Debayle (1999) and others using surface wave tomography, which incorporates azimuthal anisotropy, suggested a two-layer system of anisotropy beneath Australia: in the upper layer, directions of anisotropy are approximately oriented east–west in Debayle (1999), but more or less randomly in Simons and van der Hilst (2003). In the bottom layer, directions of anisotropy appear to be north–south, approximately parallel to absolute plate motion (APM) (Gripps and Gordon, 2002) in both models. In a more recent study, Pilia et al. (2016) related crustal azimuthal anisotropy to regional tectonics using ambient noise tomography. Their study indicated that the directions of crustal anisotropy are approximately north–south beneath mainland southeast Australia, and approximately east-west in Bass Strait and Tasmania. This result is used to carry out a comparative analysis with our results in the discussion section.

Seismic anisotropy beneath the study area has also been examined (albeit at much lower spatial resolution) through measurements of SKS/SKKS splitting for over 20 years (e.g., Vinnik et al., 1992; Girardin and Farra, 1998; Clitheroe and van der Hilst, 1998; Ozalaybey and Chen, 1999; Barruol and Hoffman, 1999; Eaton et al., 2004; Heintz and Kennett, 2005; Frederiksen et al., 2007). Of particular importance here is the study of Heintz and Kennett (2005), who used a continent wide network of 190 temporary stations with an average recording span of 6 months, which is rather limited for SWS analysis. However, the results show a complex pattern of anisotropy, which does not correlate with the contemporary plate motion direction of Argus et al. (2002). Despite the limited data availability and limited geological outcrop, especially in Phanerozoic southeast Australia which is almost entirely covered by sedimentary basins, a number of relationships were highlighted between fast polarization directions and structural trends. These relationships were interpreted to arise from anisotropy frozen into the lithosphere as a result of regional deformation events. Barruol and Hoffman (1999) studied upper mantle anisotropy using GEOSCOPE stations and attempted to explain the apparent isotropy at station “CAN”. Their study was the first to suggest an E-W anisotropic layer overlying a N-S anisotropic layer at this station. Clitheroe and van der Hilst (1998) investigated the variation in shear wave splitting across the Australian continent and showed that differing SKS splitting phenomena manifest at different frequencies, with shear wave splitting only observed at frequencies higher than 0.3 Hz. From the splitting measurements of only two stations in the neighbourhood of Tasmania, Bass Strait and adjoining southern Victoria, in which one station recorded scant S core phases and the other yielded abundant nulls, they concluded that splitting measurements in this region are either ambiguous or not well constrained.

In this paper, we present new shear wave splitting measurements across southeast Australia from both permanent seismograph stations and a recent network of temporary stations, covering a region that spans Proterozoic and Palaeozoic lithosphere. This significantly larger number of stations allows us to examine shear wave splitting variations in much more detail than has previously been possible, thus allowing us to make new inferences about the anisotropic nature of the crust and upper mantle in this region of the Tasmanides.

4. Data and methods

This study utilises seismological data from a network of 24 temporary stations that recorded for approximately 23 months (22/05/2011 to 28/04/2013) and eight permanent stations of which six are maintained by the Australian National Seismic Network (ANSN) and the remaining two are each maintained by IRIS and GEOSCOPE. The temporary stations consist of 23 Güralp 40T three-component broadband seismic stations and one Güralp CMG-3ESP broadband sensor that together span southern Victoria, several islands in Bass Strait (i.e. Flinders, King and Deal Islands) and northern Tasmania (Fig. 2). The average spacing of the temporary stations is ~80–120 km. The GSN permanent station maintained by IRIS named TAU is located in Hobart, Tasmania and has been running for ~23 years (1994-2017), while the GEOSCOPE station named CAN is located in Canberra, in mainland Australia and has been in operation since 1987 (~30 years). The six ANSN permanent stations that have been running for ~13 years are spread between Young in New South Wales and the highlands of Tasmania (Fig. 2).

We extracted data corresponding to earthquakes within epicentral distances of 85° to 140° from the centre of the network; this distance criterion is necessary to separate core S phases (SKS and SKKS) from non-radially polarized phases such as S and ScS. Visual inspection revealed that events with $M_w \geq 6.0$ provided the best signal to noise ratio and waveform clarity. Based on this, earthquakes with magnitude $M_w \geq 6.0$ were selected from the global ISC catalogue for permanent stations (Fig. 3). However, due to the shorter recording duration of the temporary stations, data from carefully selected earthquakes with magnitude $M_w \geq 5.5$ within the same epicentral distance range were also extracted for analysis.

As part of basic data pre-processing, we filtered the seismograms between 0.03 and 0.5 Hz, using a two-pole, two-pass Butterworth band-pass filter. The quality of the data was further inspected and only traces showing sharp arrivals of core phases, which are very distinct from the surrounding noise, were retained for analysis (Fig. 4).

Shear wave splitting measurements were performed on core refracted shear waves using the method of Teanby et al., (2004), which is based on the approach of Silver and Chan, (1991). Horizontal-component seismograms were rotated, with one component time shifted to minimize the second eigenvalue of the particle motion in the analysis window, thus linearising particle motion. A grid search over plausible values of φ and δt (with respective increments of 1° and 0.05 s) was performed to find the optimum solution that best removes the influence of anisotropy. A measurement window was manually picked (~10 s before SKS/SKKS arrival and ~10 s after) and individual measurements were made between the start and end time of the window. Using measurements over a set of 100 windows around the SKS or SKKS arrival, cluster analysis was then used to identify the most stable splitting parameters φ and δt corresponding to the measurement with the smallest errors.

SKS splitting results generally fall into two categories. A split wave that passes through an anisotropic medium initially shows significant energy on the tangential component and an elliptical particle motion. When the seismograms are corrected for the optimum δt and φ, the waveforms will match, the tangential component energy is minimised, and the particle motion is linearised (Fig. 5). If the seismic wave passes through azimuthally isotropic material, or if its azimuth (source polarisation) is orientated parallel or perpendicular to the fast axis of anisotropy, or if multiple layers (complex anisotropy) of anisotropy cancel out, a characteristic “null” result will be observed (Fig. 6) (e.g. Barruol and Hoffmann, 1999). In this case, there will be no energy on the tangential component prior to correction, and the uncorrected particle motion will be linear.

A single pair of splitting parameters (δt and φ) can characterise a single, horizontal and homogeneous layer of anisotropy. The presence of more complex structure, such as two or more anisotropic layers, may be indicated by systematic variations with earthquake backazimuth (Levin et al., 1999). We examined the backazimuthal coverage for SKS/SKKS phases in the study area and noted that it is not ideal, because it is heavily weighted towards events to the north and southeast of Bass Strait, which precludes a complete analysis of backazimuthal dependence of splitting parameters; this is shown in an event map (Fig. 3). Since the dataset contains this restriction, the presence of multiple anisotropic layers cannot be reliably inferred.

5. Results

We categorise individual shear wave splitting results based on: (1) the quality of the initial signal; (2) a clear separation between the fast and slow shear wave before transverse energy minimisation; (3) the ellipticity of the particle motion in the horizontal plane before transverse energy minimisation; (4) the linearisation of particle motion after transverse energy minimisation; and (5) the waveform coherence between the fast and slow split shear waves. We identified "good" measurements as those that satisfy the following criteria: (i) high waveform clarity; (ii) elliptical initial particle motion and linear or nearly linear particle motion after correction; (iii) splitting parameter estimates that were consistent within error along with fairly small error ellipses; and (iv) with errors less than ±10° in the fast direction and ± 0.20s in delay time. Measurements meeting only three criteria with larger error bars (up to ± 20° in φ and ± 0.30s in δt) and lower waveform clarity were marked as "fair". A poor measurement only fulfils two criteria and null measurements were identified by an initial linear particle motion and a lack of energy on the transverse component associated with the arrival of the core phase of interest on the radial component. An example of high-quality splitting and null measurements are shown in Figure 5 and 6, respectively.

After applying the splitting measurement procedure described in the previous section, a total of ~366 well-constrained measurements of φ and δt at 24 temporary and 8 permanent stations were obtained. Out of these, ~51 were classified as "good" and ~109 as "fair" In addition to these, ~206 high-quality ("good"+"fair") null measurements were identified. Some individual stations had 4–8 "good" quality measurements, while others had $\leq$3. At several stations the measurement procedure only yielded "fair" quality measurements and in some cases only "null" measurements were produced. This modest return of good results is consistent with previous shear wave splitting studies in the region.

The shear wave splitting parameter measurements (Fig. 7) were generally found to cluster relatively tightly around certain dominant directions. For this reason, despite long recording times at some of the stations, the measurements are largely confined to two or three relatively restricted back azimuthal ranges (Fig. 7). As noted earlier, the large gaps in azimuthal coverage do not allow for a direct interpretation of multi-layered anisotropic characteristics; therefore, we restrict our quantitative analyses to comparisons with the dominant anisotropic directions inferred from the full sets of measurements. A notable exception is station CAN in the northeastern part of the study area. The back azimuthal coverage here is slightly better than average, but almost two-thirds of the measurements indicate null results.

In order to present a clear first-order picture of SKS splitting patterns beneath the study area, we took a weighted mean of splitting parameters (φ, δt) for each station (Fig. 8)(splitting parameters can be found in the supplementary data). This represents an average value that weighs each individual non-null measurement by its value of φ and δt error bars. Good splits that generally have smaller error bounds are given more weight so that they contribute to the weighted mean more than fair splits. For the fast polarisation, this is done by averaging angles of the whole set of measurements (good and fair) as points on a unit circle in a Cartesian plane and then converting it back. The weighted means of splitting parameter values can be found in Table 1, with a plot of the resulting splitting orientations and delay times, and a histogram station performance indicated by the number of measurements at individual stations, shown in Figures 8 and 9 respectively.

There are some regional trends that are evident from Figure 8. First, the dominant splitting orientations range from NE-SW to NW-SE within a broadly N-S average. We note significant changes in splitting orientation between individual stations spaced ~300 to 500 km apart. Delay times are also highly variable, ranging from the smallest δt in Bass Strait of ~0.66±0.10s (BA01) to the largest δt in southern Victoria of ~2.70±0.25s (BA18). Despite the spatial variability in fast direction and delay time, some correlation can still be seen when looking at the results more closely, especially in: (1) the Lachlan Fold Belt (Eastern Lachlan Orogen); (2) the postulated micro-continent VanDieland; (3) East Tasmania Terrane (ETT) and Furneaux Islands; and (4) the Newer Volcanics Province.

In the Lachlan Fold Belt (Fig. 8), moderate to large delay times occur over the range 0.73±0.13 s (CNB) to 2.47±0.25 s (BA12) with a dominant approximate fast direction of NNE-SSW. These fast directions are sub-parallel to the structural trend of the Lachlan Fold Belt. One station of note here (CAN), which will be discussed in more detail later, has unusual splitting parameters. At this station, only fair measurements have been observed and the overall splitting measurement comprises abundant nulls from all backazimuths. In VanDieland there is a broad NE-SW variation in the fast direction from southern Victoria to western Tasmania. It is observed that stations in southern Victoria exhibit significant shear wave splitting, with average delay times at individual stations between ~1.15±0.24 s (BA21) and ~2.70±0.25 s (BA18) and an approximate fast direction of N-S to NE-SW. At the Bass Strait islands that form part of VanDieland, delay times are comparatively small (~0.66±0.10 s (BA01) to ~1.43±0.08 s (BA10)), with fast directions oriented in a roughly NE-SW direction. At the southern end of the micro-continent (western Tasmania), all observed fast directions are approximately NE-SW while the delay time is in the range ~0.74±0.13 s (BA02) to ~1.68±0.21 s (BA04). Looking at stations in the centre of southern Tasmania (MOO and TAU), the splitting measurements are in the range ~1.67±0.22 s (MOO) to ~2.07±0.43 s (TAU) and fast direction orientation is also approximately NE-SW.

The observed fast shear wave splitting directions for the East Tasmania Terrane (ETT) and Furneaux Islands show that the fast directions rotate from NW-SE in the East Tasmania Terrane (BA05, BA06) to E-W in the Furneaux Islands (BA07, BA08, BA09) and a delay time range of ~0.68±0.05 s to ~2.14±0.32 s is observed. Interestingly, the concentration of large delay times delineates a region in the heart of the Newer Volcanics Province (NVP) (Fig. 8). Some stations surrounding the NVP exhibit somewhat larger delay times than more distant stations.

The splitting pattern shown in Figure 8 is largely consistent with results from previous studies of shear wave splitting in south east Australia (e.g., Heintz and Kennett, 2005), although the data set described here has a much longer recording duration and spatial resolution. The pattern of fast directions found in our study region is also generally consistent with the larger-scale splitting pattern observed across the Australian continent (e.g., Clitheroe and van der Hilst, 1998; Heintz and Kennett, 2005; Barruol and Hoffman, 1999).

6. Discussion

The main challenge in studying core-refracted shear waves is the lack of vertical resolution due to near vertical paths of the SKS/SKKS phase through the upper mantle. The anisotropy measured at the surface has been acquired between the core-mantle boundary (CMB) and the surface; the splitting parameters therefore represent a path-integrated measurement and a key question is whether the splitting observed in the study area reflects anisotropy in the crust, in the mantle lithosphere (reflecting past deformational episodes), in the asthenosphere (related to present-day mantle flow), or a combination of these factors. If we consider an asthenospheric source of anisotropy, the mantle flow can be of two types: passive (Couette flow) and active (Poiseulle flow) (Stotz et al., 2017, 2018). Couette flow is generated in the asthenosphere by overlying plate motion; the associated horizontal shear stresses cause asthenospheric deformation beneath the plate. On the other hand, Poiseulle flow is driven by internal forces (pressure gradient) within the asthenosphere, such that flow velocities peak in the middle of the asthenospheric channel. Studies show that these two forces can occur together and any asthenospheric flow pattern is a linear combination of Couette and Poiseulle flow pattern (Stotz et al., 2018). If the source of the observed anisotropy is considered to be the asthenospheric flow, then this can lead to coherent splitting parameters over scale lengths >600 km (Becker et al., 2007). In this situation, the orientation of the polarisation plane of the fast shear wave would be parallel to the Absolute Plate Motion (APM) direction (Tommasi, 1998). However, our results neither indicate very coherent splitting parameters over large regions nor alignment of fast shear wave with APM direction. This will be investigated in more detail below.

6.1 Implications for plate tectonic evolution in SE Australia

At stations located in the Lachlan Fold Belt (CNB, CAN, BA12, BA13, BA14, BA15, BA16, BA19, DLN, YNG), the relative contributions to the observed splitting from the crust, mantle lithosphere, and asthenosphere are difficult to characterise due to poor backazimuthal coverage of the data. However, the direction of anisotropy is parallel to the structural trend of the Lachlan Fold Belt i.e. NE-SW (Stations BA12, BA14, BA15, BA16 CNB, DLN, YNG). These measurements may be caused by fossil anisotropy in the lithosphere sourced from deformation-induced alignment of minerals related to the formation of the Palaeozoic Lachlan Fold Belt. However, we note that at 145°E and 38°S, the plate motion is approximately 59 mm/yr in the direction N20°E (estimated from NNR-MORVEL56 – see Argus et al., 2011), which means that a significant contribution from the sublithospheric mantle cannot be ruled out. Measurements performed at CNB are similar to those obtained by Clitheroe and Van der Hilst (1998), accounting for a weighted mean average of $\delta t = 1.40 \pm 0.06$s and $\varphi = 38 \pm 6°$ that coincides with the NE-SW trend of the Lachlan Fold Belt.

At GEOSCOPE station CAN, clear evidence was found for either NE-SW or NW-SE oriented φ. These findings are consistent with a two-layer model, as suggested by Barruol and Hoffmann (1999), in which the two layers have roughly similar δt and anisotropy in each layer has a perpendicular orientation with respect to the adjacent layer. The anisotropic φ of the lower layer is roughly parallel (approximately northward) to the current plate motion direction. This model is supported by results from surface wave tomographic studies (e.g. Debayle and Kennett, 2000), which reported a change in anisotropic pattern at approximately 150 km depth. Moreover, in another study focussing on this particular station, Girardin and Farra (1998) suggested a two-layer model, where the 140 km upper layer has a roughly EW oriented φ and a 40 km thick lower layer with a N-S φ parallel to the current plate motion direction. CAN also has abundant and good back-azimuthal coverage of nulls, indicating either the absence of anisotropy along the ray path or that the fast polarisation is orthogonal to the direction of anisotropy (Fig. 10). Silver and Savage (1994) pointed out that apparent isotropy may be consistent with a simple two-layer model, where the two layers exhibit the same intrinsic and mutually perpendicular fast directions. Here, the medium may either be isotropic or the initial polarisation is parallel to the fast or slow direction of anisotropy for that propagation direction. Although the structure at station CAN is illuminated by a relatively better backazimuthal coverage, shear wave splitting observations suggest dominance of usable events arriving at a backazimuth around N0-N30°E and N120-N180°E. This station also exhibits a significant variation in both delay time and fast polarisation direction with backazimuth and well constrained nulls were identified over a large swath of backazimuths; such a pattern is consistent with complex anisotropic structure beneath a station (e.g. Silver and Savage, 1994). In an ideal case of a simple, horizontal two-layered structure the apparent anisotropy parameters should vary with a $\pi/2$ periodicity. This is not the case with the station CAN and all other stations within the Lachlan Orogen; hence other factors like dipping structures or lateral heterogeneity may be present. Overall, splitting patterns at individual stations in this region are often complicated, which implies that the anisotropic structure beneath this region is also complex. This reinforces a likely contribution from several different regions of the crust and/or upper mantle that augment or cancel each other out.

Elsewhere on mainland Australia in our study region, there are three stations (BA23, BA24 and MILA) where no reliable measurements have been found except for several coherent null measurements. Whether this is a true reflection of anisotropic structure in this region is difficult to tell because these stations are generally characterised by poor quality data.

The splitting pattern in the microcontinent (VanDieland) can be divided into two groups: (1) Western Tasmania Terrane (WTT); and (2) the Selwyn Block (the northward extension of west Tasmania that spans Bass Strait and penetrates beneath central Victoria) and submerged continental crust adjacent to Tasmania. In the WTT, stations BA01, BA02, BA03 have a NE-SW direction of fast polarisation that ranges from $38\pm3^\circ$ to $65\pm3^\circ$. The stations highlight some correlation between fast shear wave polarisation directions and the trend of the dominant surface structures; however, it shows a poor correlation with APM (~N20°E) and thus asthenospheric flow, while it could be one of the main causes, cannot be considered as the principal cause of the observed anisotropy. These stations (WTT) and the stations in the northeast of Tasmania (ETT) (BA04, BA05, BA06) have similar attributes in terms of correlation between fast shear wave polarisation direction and the trend of dominant surface structures as well as poor correlation with APM except that the dominant fast polarisation direction north east of Tasmania (ETT) is NW-SE ($-48\pm3^\circ$ to $-86\pm4^\circ$). Our mean splitting measurement from the permanent GSN station TAU located in Hobart, southern Tasmania, agrees well with past SWS studies of Vinnik et al. (1989) and Clitheroe and van der Hilst (1998). The results show that the fast shear wave polarization direction is approximately

ENE-WSW and parallel to the trend of the dominant surface structures in the area. These structures are likely related to a later phase of the Cambrian Tyennan Orogeny (Corbett et al., 1972), which represents the first phase of orogeny along the East Gondwana margin as a result of westward subduction of the Palaeo-Pacific plate. Another station "MOO" adjacent to TAU exhibits similar splitting parameters and together this may indicate that the lithosphere is the principal cause of the observed anisotropy in this region.

Moving northward into Bass Strait and south central Victoria (Selwyn Block), the systematic variation of strength and orientation of anisotropy across the stations (BA10, BA11, BA17, BA19, BA20, BA21, TOO) provides insight into how complex the tectonics of this region may have been. Few reliable splitting measurements were observed on King and Deal Islands owing to the low quality of the signal. Other possible contributing factors include the presence of complex upper mantle structures beneath the stations, including compositionally heterogeneous Selwyn Block (Cayley et al., 2002), and magma-induced heating of the upper mantle associated with the recent Quaternary Newer Volcanics Province. However, despite the fact that recent deformational events associated with breakup between Australia and Antarctica have possibly reworked previous anisotropy imprints, it is generally observed that splitting measurements in northwestern Tasmania through King Island to the southern tip of Victoria have a roughly similar fast polarisation direction of NE-SW. This trend is strongly correlated with magnetic signatures that can be traced from northwestern Tasmania to southern Victoria and are thought to be inherited from the Selwyn Block (Cayley et al., 2002). This suggests a tectonic affinity of the Selwyn block and northwest Tasmania and appears to support the presence of the so-called exotic Precambrian microcontinent VanDieland (Cayley, 2011; Moresi et al., 2014; Pilia et al., 2015b). We speculate that the microcontinent behaved as a rigid block, where the separation between Australia and Antarctica was forced to propagate along the Sorrel Fault System, preventing pervasive deformation of the microcontinent and retaining a substantially intact pattern of anisotropy since the Mesoproterozoic (Cayley, 2011). However, we note that our ability to retrieve a reliable anisotropy signature may be reduced by the lower signal to noise ratio of the Bass Strait islands dataset.

Stations BA05, BA06, BA07, BA08, BA09 and BA17 collectively indicate a rotation in fast shear wave polarisation directions from NW-SE in the ETT (BA05, BA06) to NE in the Furneaux Islands (BA07, BA08). This discrepancy between the ETT and the Furneaux Islands may be due to the relatively recent breakup of Australia and Antarctica, which resulted in lithospheric thinning, and subsequent formation of the three intracratonic rift basins in Bass Strait that host the Furneaux Islands (Gunn et al., 1997; Gaina et al., 1998; Fishwick and Rawlinson, 2012). Smaller delay times at the Furneaux Island stations (~0.82±0.07 s (BA08) and ~0.68±0.06 s (BA09)) appear to suggest a positive correlation with lithospheric thickness in this region (Kennett and Blewett, 2012; Fishwick et al., 2008). In spite of this apparent correlation, there appears to be no correlation between the fast polarisation direction and the absolute plate motion. Hence, anisotropy beneath ETT and the Furneaux Islands appears to be primarily caused by fossil deformation recorded in the lithosphere.

Our results demonstrate that the average delay times observed in southern Victoria are considerably higher than in other parts of the study area. Measurements in the vicinity of the Newer Volcanics Province (NVP) in southern Victoria show unusually large delay times for which a primary contribution from the asthenospheric mantle is likely (e.g. Long et al., 2009). Two possible scenarios that would result in unusually high delay times are: (1) having an unusually thick anisotropic layer beneath the NVP. Because shear wave splitting is inferred to be due to Lattice Preferred Orientation (LPO) of olivine in the asthenospheric mantle, it is plausible that the thin lithosphere beneath the NVP is associated with a correspondingly thick asthenosphere; (2) differences in upper mantle temperatures make olivine LPO particularly strong in the anisotropic layer beneath the NVP (Karato et al., 2007). Because of the large observed delay times, a model in which all of the anisotropy is in the crust and mantle lithosphere would imply an unreasonably large magnitude of anisotropy (roughly 20% anisotropy for a ~60 km thick lithosphere) and we can confidently infer that the large delay times reflect contemporary flow in the asthenospheric mantle (Rawlinson et al., 2017). While a small contribution to the observed splitting from crustal anisotropy is likely, average values predicted from rock physics for crustal splitting are on the order of perhaps ~0.1–0.3 s (Herquel et al., 1994; Savage, 1999). Maximum delay times of 0.1 to 0.2 s per 10 km of homogeneously deformed crust might be expected (Barruol and Mainprice, 1993). This could generate crustal delay times of up to ~0.8 s in southeast

Australia. Thus the large delay times observed here cannot be attributed primarily to crustal anisotropy. Even if we attribute 1 s of delay time to anisotropy in the crust and mantle lithosphere, the asthenosphere would have to contribute 1.5–2s of splitting beneath the NVP, which corresponds to ~6–8% anisotropy for a 150-km thick asthenosphere. Although these values are quite large compared to 3%, a value considered reasonable for a normal upper mantle, they are not out of the question. For example, Ben Ismaïl and Mainprice (1998) reported shear wave anisotropies larger that 11% and up to 15% in the upper mantle. However, these values were calculated for pure olivine crystals and they should reduce somewhat when the effect of 25–30 % of pyroxenes in lherzolites is taken into account (e.g., Mainprice and Silver, 1993).

Although we have largely interpreted the shear wave splitting results in terms of anisotropy frozen in the lithosphere and asthenospheric flow due to plate motion, we also consider an intriguing alternative in which we investigate φ as a function of angle by looking at results from stations surrounding Bass Strait. The overall fast polarisation direction appears to radiate outwards from the centre of Bass Strait. This observation could potentially be consistent with divergent mantle flow for a plate overriding a mantle plume. According to the plume theory (Wilson, 1963; Morgan, 1971), since the fast directions of anisotropy are determined by the spreading direction of the mantle, the fast polarisation directions (φ) of anisotropy around a mantle plume would be oriented vertically within the central upwelling and radiate outwards from the plume head (Rümpker and Silver, 2000; Ito et al., 2014). For example, Walker et al. (2001) studied shear wave splitting around the Hawaii hotspot and observed a spatial pattern in fast polarisation directions that they explained in terms of a parabolic asthenospheric flow model, in which a plume impinges on a moving lithospheric plate. Walker et al. (2005) invoked similar models to explain a semicircular pattern of fast polarisation directions in the vicinity of the Eifel hotspot and to explain the spatial distribution of fast polarisation directions in the eastern Snake River Plain adjacent to the Yellowstone hotspot (Walker et al., 2004). With the superimposed influence of absolute plate motion, horizontal flow away from the central plume head upwelling is predicted to be parabolic (Walker et al., 2005). This is a model that combines the effect of mantle upwelling with APM, resulting in parabolic flow in the asthenosphere, and has been successful at explaining patterns of fast polarisation directions in some regions associated with mantle upwelling, but has proved less successful in regions such as Afar (Gashawbeza et al., 2004;

Walker et al., 2005) or Iceland (Walker et al., 2005).

Previous studies by Davies et al. (2015) identify the world's longest continental hotspot track (over 2000 km long) which begins in north Queensland, and extends southward, possibly as far as NW Tasmania. The plume source of the hotspot track may be responsible for the observed pattern of fast polarisation directions surrounding Bass Strait. However, further evidence would be required if such a theory was to gain traction; apart from plate motion model predictions of the current plume source, there is very little evidence to suggest that it still exists, apart from reduced uppermost mantle velocities imaged by regional surface wave tomography (Fishwick and Rawlinson, 2012). Recent studies indicate that the plume waned during its traverse of the Australian continent, and it may now have dissipated completely (Rawlinson et al., 2017).

Overall, the complicated SKS waveforms and splitting patterns observed in the study area are plausibly due to multiple layers of anisotropy, asthenospheric contribution to the anisotropy, considerable lateral heterogeneity, complex lithospheric keels (i.e., Vinnik et al., 1989, 1992; Barruol and Hoffmann, 1999; Heintz and Kennett, 2005), or a combination of these factors. Without detailed modelling, which the backazimuthal coverage will not permit, it is difficult to untangle the relative contributions to the observed splitting from the lithospheric vs. asthenospheric upper mantle, but we can say with confidence that the lithosphere and/or crust likely makes a significant contribution to the splitting signal in this region.

6.2 Comparison with magnetic anomalies

Despite the limited number of reliable measurements obtained at some stations largely due to high noise levels, particularly in the island stations in Bass Strait and northern Tasmania, direct correlations can still be observed between the measured orientation of the polarization plane of the fast shear-waves and the mapped near-surface structures from the magnetic data (Fig. 11). The NE-SW linear structures of alternating positive and negative magnetic anomalies in northwest Tasmania are presumed to represent magmatic dikes of the Mount Reid Volcanics (Crawford et al., 2003; Berry, 1995; Seymour et al., 2007). There is a good correlation between fast shear wave splitting directions (φ) and magnetic lineaments in NW

Tasmania. However, ETT and Furneaux Islands are devoid of any correlation between fast shear wave splitting directions (φ) and magnetic lineaments, which are considerably weaker compared to those observed in eastern Bass Strait. In the Lachlan Orogen, the magnetic anomalies and fast shear wave splitting directions (φ) are parallel to the structural trend of the Lachlan Fold Belt. However, the correlation in southern Victoria and the Bass Strait islands is poor.

Magnetic anomalies reflect a contrast in upper crustal composition and/structural fabric (Kletetschka and Stout, 1998). An alignment between fast splitting directions (associated with the upper mantle) and crustal magnetic lineaments thus implies the presence of vertically coherent deformation (VCD). This helps support the idea that anisotropy frozen in the lithosphere is the main source of anisotropy in this region.

6.3 Comparison with crustal anisotropy measurements from surface wave tomography

One of the well-known limitations of shear-wave splitting analysis is its inability to resolve the depth distribution of anisotropy. By contrast radial variations in anisotropy can be assessed by surface wave data, which samples different depth ranges as a function of period. However, surface wave anisotropy measurements have significantly poorer lateral resolution than shear wave splitting measurements. Despite the fact that these two measurements do not identically sample the lithosphere, we believe that a comparison of our splitting measurements with the crustal anisotropy measurements of Pilia et al. (2016) will shed more light on the characteristics of the anisotropy in our study area (Fig. 12). Upon comparing the weighted mean of SKS/SKKS splits with the 5 second period Rayleigh wave phase anisotropy variations in the crust, it can be seen that the fast polarisation direction (φ) along the Lachlan Fold Belt and southern Victoria are quite consistent; this supports our earlier contention that lithospheric anisotropy is envisaged to be the dominant contributor in this region. In Bass Strait the φ measurements seem to be quite consistent in both models. It is interesting to note that measurements in Tasmania have 90° inconsistencies in φ. Even though this anomaly did not manifest when comparing our results with magnetic structures, crust-mantle decoupling cannot be completely ruled out. Another, perhaps more likely, interpretation is that the surface wave anisotropy is restricted to the upper crust, and therefore does not dominate the shear wave splitting signal.

7. Conclusions

New results from the shear wave splitting data set presented in this study provide a first-order picture of anisotropy and deformation in the upper mantle beneath Bass Strait and the adjoining land masses and yields constraints on the different tectonic terranes in southeast Australia. Despite uneven station distribution, noisy data recorded on the islands in the study area, and a complex tectonic history, we were able to highlight coherent patterns of anisotropy from shear wave splitting in different parts of the study area.

Evidence of fast shear wave splits being polarised in directions oriented parallel to the local structural trends (e.g. northwest Tasmania and Selwyn Block and along the Lachlan Fold Belt) may account for deformation induced LPO anisotropy frozen in the lithosphere. The strong anisotropy observed beneath NVP possibly reflects an anisotropy contribution from thick asthenosphere underlying a thin lithosphere. The overall fast polarisation that appears to radiate outwards from the centre of Bass Strait could alternatively be the result of plume-induced anisotropy, although we acknowledge that evidence for a plume in this region is limited. However, based on evidence from various sources including crustal surface wave tomography, it is difficult to interpret the occurrence of complex patterns of anisotropy and abnormally large delay times from shear wave splitting beneath southeast Australia in terms of either mantle-flow related anisotropy or anisotropy frozen in the lithosphere: a contribution from both the lithospheric and sublithospheric mantle is likely. The poor backazimuthal coverage is not sufficient to be able to pin down the contribution from each source of anisotropy by, for instance, performing two-layer modelling of the anisotropy.

In an attempt to understand the depth-distribution of anisotropy we compared the observed fast polarisation directions with other datasets: (1) the fast polarisation directions vary for each tectonic unit, indicating a dominant lithospheric "fossil" anisotropy. This interpretation is supported by (2) poor correlation of fast polarisation direction with plate motion direction, which may be parallel only by chance at a few stations and thus does not reflect large scale asthenospheric process; (3) the trend of magnetic structures aligns well with the observed fast polarisation directions at many of the analysed stations. This suggests vertically coherent deformation throughout the crust and upper-most mantle and supports the idea that splitting measurements reflect the most recent tectonic event; (4) there is also a consistency between (crustal) azimuthal anisotropy directions and our teleseismic shear wave splitting fast polarisation directions in mainland Australia and Bass Strait, but the anisotropy directions of the two different measurements appear to be roughly orthogonal in Tasmania. Even though this anomaly did not manifest in the comparison of our results with magnetic structures, crust-mantle decoupling cannot be completely ruled out. Alternatively, the pattern of surface wave anisotropy observed may simply be an upper crustal feature, and hence only makes a small contribution to the shear wave splitting signal which is otherwise dominated by the lower crust and upper mantle.

Acknowledgements

The work contained in this paper was conducted during a PhD study funded by Abubakar Tafawa Balewa University, Bauchi, Nigeria and University of Aberdeen, UK. We thank field teams working through UTAS and ANU, and Armando Arcidiaco and Qi Li, ANU, for assistance with collection and archiving of the BASS data used in this study. Australian Research Council grant LP110100256 was instrumental in supporting the BASS deployment. We also thank Geoscience Australia and IRIS for providing part of the data used in this study.

References

Argus, D. F., Gordon, R. G. & DeMets, C. (2011). Geologically current motion of 56 plates relative to the no-net-rotation reference frame. Gechemistry, Geophysics, Geosystems 12, Q11001, DOI:10.1029/2011GC003751.

Barbuska, V. & Cara, M. (1991). Seismic anisotropy in the Earth. Kluwer Academic Publishers, 1991, 217 pp.

Barruol, G. & Hoffman R. (1999). Seismic anisotropy beneath the Geoscope stations from SKS splitting. Journal of Geophysical Research 104, 10757–10774.

Bastow, I., Owens, T., Helffrich, G. & Knapp, J. (2007). Spatial and temporal constraints on sources of seismic anisotropy: Evidence from the Scottish highlands. Geophys. Res. Lett. 34, L05305, DOI:10.1029/2006GL028911.

Becker, T. W., Browaeys, J. T. & Jordan, T. H. (2007). Stochaastic analysis of shear-wave splitting length scales. Earth and Planetary Sci. Letters 259, 526-540.

Berry, R. F. (1995). Tectonics of western Tasmania: Late Precambrian–Devonian, in: COOKE, D. R.; KITTO, P. A. (ed.). Contentious issues in Tasmanian geology. Abstracts Geological Society of Australia 39, 6–8.

Berry, R. F., Chmielowski, R. M., Steele, D. A. & Maffre, S. (2007). Chemical U – Th – Pb monazite dating of the Cambrian Tyennan Orogeny, Tasmania. Australian Journal of Earth Sciences 54:5, 757-771, DOI: 10.1080/08120090701305269.

Ben Ismaïl, W. & Mainprice, D. (1998). A statistical view of the strength of seismic anisotropy in the upper mantle based on petrofabric studies of ophiolite and xenolith samples. Tectonophysics 296, 145–157.

Betts, P.G., Giles, D. Lister, G.S. & Frick, L.R. (2002). Evolution of the Australian lithosphere. Aust. J. Earth Sci. 49, 661 – 695.

Berry, R. F. & Crawford, A. J. (1988). The tectonic significance of Cambrian allochthonous mafic-ultramafic complexes in Tasmania. Australian Journal of Earth Sciences 35, 523–533.

Black, L. P., McClenagan, M. P., Korsch, R. J., Everard, J. L., Calver, C. R., Seymour, D. B., Reed, A. & Foudoulis, C. (2004). Using SHRIMP to decipher the history of middle Paleozoic magmatism in Tasmania. Geological Society of Australia Abstracts v. 73, 55.

Blackman, D. & Kendall, J. -M. (1997). Sensitivity of teleseismic body waves to mineral texture and melt in the mantle beneath a mid-ocean ridge. Philos. Trans. R. Soc. A, 355, 217–231, DOI:10.1098/rsta.1997.0007.

Burton, G. R., & Triggs, S. J. (2014). Discussion of Glen R. A., Korsch R. J., Hegarty R., Saeed A., Poudjom Djomani Y., Costelloe R. D. & Belousova E. (2013). Geodynamic significance of the boundary between the Thomson Orogen and the Lachlan Orogen, northwestern New South Wales and implications for Tasmanide tectonics. Australian Journal of Earth Sciences 60, 371–412. Australian Journal of Earth Sciences 61:4, 639-641, http://dx.doi.org/10.1080/08120099.2014.903857

Cayley, R. (2011). Exotic crustal block accretion to the eastern Gondwanaland margin in the Late Cambrian–Tasmania, the Selwyn Block, and implications for the Cambrian–Silurian evolution of the Ross, Delamerian, and Lachlan orogens. Gondwana Research, 19, 628–649. http://dx.doi.org/10.1016/j.gr.2010.11.013.

Cayley R., Taylor, D. H., VandenBerg, A. H. M. & Moore, D. H. (2002). Proterozoic Early Palaeozoic rocks and the Tyennan Orogeny in central Victoria: the Selwyn Block and its tectonic implications. Australian Journal of Earth Sciences 49, 225 – 254.

Clitheroe, G. & van der Hilst, R. (1998). Complex anisotropy in the Australian lithosphere from shear wave splitting in broadband records. AGU Geophysical Monographs.

Corbett, K. D., Banks, M. R. & Jago, J. B. (1972). Plate tectonics and the Lower Palaeozoic of Tasmania, Nature Phys. Sci. 240, 9 – 11.

Crampin, S. (1994). The Fracture criticality of crustal rocks. Geophys. J. Int. 118, 428-438.

Crawford, A. J. & Berry, R. F. (1992). Tectonic implications of Late Proterozoic–Early Palaeozoic igneous rock associations in western Tasmania. Tectonophysics 214, 37–56.

Crawford, A., Meffre, S. & Symonds, P. (2003). 120 to 0 Ma tectonic evolution of the southwest Pacific and analogous geological evolution of the 600 to 220 Ma Tasman Fold Belt System. Special Papers—Geological Society of America, 383–404.

Davies, D.R., Rawlinson, N., Iaffaldano, N. & Campbell, I.H. (2015). Lithospheric controls on magma composition along Earth's longest continental hotspot track. Nature 525, 511–514.

Debayle, E. & Kennett, B.L.N. (1998). Anisotropy in the Australian upper mantle from waveform inversion, Ann. Geophys. 16, 37.

Debayle, E. & Kennett, B.L.N. (2000). The Australian continental upper mantle: Structure and deformation inferred from surface waves, J. Geophys. Res. 105, 25423-25450. DOI:10.1029/2000JB900212.

Debayle, E. (1999). SV-wave azimuthal anisotropy in the Australian upper mantle: preliminary results from automated Rayleigh waveform inversion, Geophys. J. Int. 137, 747 – 754.

Direen, N.G. & Crawford, A.J. (2003). The Tasman Line: where is it, what is it, and is it Australia's Rodinian breakup boundary? Australian Journal of Earth Sciences 50, 491–502. http://dx.doi.org/10.1046/j.1440-0952.2003.01005.x.

Eaton, D., Frederiksen, A. & Miong, S.-K. (2004). Shear-wave splitting observations in the lower Great Lakes region: Evidence for regional anisotropic domains and keel-modified asthenospheric flow, Geophys. Res. Lett. 31, L07610, DOI:10.1029/2004GL019438.

Elliot, C. G., Woodward, N., B. & Gray, D. R. (1993). Complex regional fault history of the Badger Head region, northern Tasmania. Aust. J. Earth Sci. 40, 155 – 168.

Fergusson, C. L. (2009). Tectonic evolution of the Macquarie Arc, central New South Wales. Arguments for subduction polarity & anticlockwise rotation. Australian Journal of Earth Sciences 56, 179 - 193.

Fergusson, C. L. (2014). Discussion on ‘Refining accretionary orogen models for the Tasmanides of eastern Australia’ by R. A. Glen. Australian Journal of Earth Sciences 61. DOI:10.1080/ 08120099.2014.917334.

Fishwick, S., Heintz, M., Kennett, B. L. N., Reading, A. M. & Yoshizawa, K. (2008). Steps in lithospheric thickness within eastern Australia, evidence from surface wave tomography. Tectonics v. 27, TC0049, DOI: 10.129/2007TC002116.

Fishwick, S. & Rawlinson, N. (2012). 3-D structure of the Australian lithosphere from evolving seismic datasets. Australian Journal of Earth Sciences 59, 809-826.

Foster, D. A. & Gray, D. R. (2000). Evolution and structure of the Lachlan Fold Belt (Orogen) of eastern Australia. Annual Reviews of Earth and Planetary Sciences 28, 47 – 80.

Fouch, M. J., Fischer, K. M., Parmentier, E., Wysession, M. E. & Clarke, T. J. (2000). Shear wave splitting, continental keels, and patterns of mantle flow. J. Geophys. Res. 105(B3), 6255–6275, DOI:10.1029/1999JB900372.

Frederiksen, A., Miong, S.-K., Darbyshire, F., Eaton, D., Rondenay, S. & Sol, S. (2007). Lithospheric variations across the Superior Province, Ontario, Canada: Evidence from tomography and shear wave splitting. J. Geophys. Res. 112, B07318, DOI:10.1029/2006JB004861.

Gaina, C., Muller, D., Royer, J. -Y., Stock, J., Hardebeck, J. & Symonds, P. (1998). The tectonic history of the Tasman Sea: a puzzle with 13 pieces. J. Geophys. Res. 103, 12,413-12,433.

Gashawbeza, E. M., Klemperer, S. L., Nyblade, A. A., Walker, K. T. & Keranen, K. M. (2004). Shear-wave splitting in Ethiopia: Precambrian mantle anisotropy locally modified by Neogene rifting, Geophys. Res. Lett. 31, L18602. http://dx.doi.org/ 10.1029/2009JB007141.

Graeber, F. M., Houseman, G. A. & Greenhalgh, S. A. (2002). Regional teleseismic tomography of the western Lachlan Orogen and the Newer Volcanic Province, southeast Australia. Geophy. J. Int. 149, 249–266.

Girardin, N. & Farra, V. (1998). Azimuthal anisotropy in the upper mantle from observations of P-to-S converted phases: Application to southeast Australia. Geophys. J. Int. 133, 615-629.

Glen, R. A. (2005). The Tasmanides of eastern Australia. In A. P. M. Vaughan, P. T. Leat, & R. J. Pankhurst (Eds.), Terrane processes at the margins of Gondwana (Vol. 246. pp. 23-96). London: Geological Society, London, Special Publication.

Glen, R.A. (2013). Refining accretionary orogen models for the Tasmanides of eastern Australia. Aust. J. Earth Sci. 60, 315–370.

Glen, R. A., Poudjom Djomani, Y. H., Belousova, E., Hegarty, R. & Korsch, R. J. (2014). Geodynamic significance of the boundary between the Thomson Orogen and the Lachlan Orogen, northwestern New South Wales and implications for Tasmanide tectonics: Reply. Australian Journal of Earth Sciences 61, 643-657.

Gray, D. R. & Foster, D. A. (2004). Tectonic evolution of the Lachlan Orogen, southeastern Australia: historical review, data synthesis and modern perspectives. Australian Journal of Earth Sciences 51, 773-817.

Gripp, A.E. & Gordon, R.G. (2002). Young tracks of hotspots and current plate velocities. Geophys. J. Int. 150, 321 – 361.

Heintz, M. & Kennett, B. L. N. (2005). Continental scale shear wave splitting analysis: Investigation of seismic anisotropy underneath the Australian continent. Earth and Planetary Science Letters 236, 106–119.

Herquel, G., Wittlinger, G. & Guilbert, J. (1995). Anisotropy and crustal thickness of Northern-Tibet. New constraints for tectonic modelling, Geophys. Res. Lett. 22, 1925-1928.

Holm, O. H., Berry, R. F. (2002). Structural history of the Arthur Lineament, northwest Tasmania: an analysis of critical outcrops. Australian Journal of Earth Sciences 49, 167–185.

Ito, G., Dunn, R., Li, A., Wolfe, C. J., Gallego, A. & Fu, Y. (2014). Seismic anisotropy and shear wave splitting associated with mantle plume-plate interaction, J. Geophys. Res. Solid Earth 119, DOI:10.1002/2013JB010735.

Karato, S., Jung, H., Katayama, I. & Skemer, P. (2008). Geodynamic significance of seismic anisotropy of the upper mantle: new insights from laboratory studies, Annual Rev. Earth Planet. Sci. 36, 59-95.

Kennett, B. L. N., & Blewett, R. S. (2012). Lithospheric framework of Australia, Episodes Vol. 35(1), 9-22.

Kletetschka, G. & Stout, J. H. (1998). The origin of magnetic anomalies in lower crustal rocks, Labrador. Geophys. Res. Letters Vol. 25, No. 2, 199-202.

Leaman, D., Baillie, P. & Powell, C.M. (1994). Precambrian Tasmania: a thin-skinned devil. Exploration Geophysics 25, 19–23. DOI:10.1071/EG994019.

Levin, V., Menke, W. & Park, J. (1999). Shear wave splitting in the Appalachians and the Urals: A case for multilayered anisotropy. J. Geophys. Res. 104, 17, 975–17,993, DOI:10.1029/1999JB900168.

Lister, G.S., Ethridge, M.A. & Symonds, P.A. (1991). Detachment models for the formation of passive continental margins. Tectonics 10, 1038–1064.

Long, M. D., Gao, H., Klaus, A., Wagner, L. S., Fouch, M. J., James, D. E. & Humphreys, E. (2009). Shear wave splitting and the pattern of mantle flow beneath eastern Oregon. Earth and Planetary Science Letters 288, 359–369.

Long, M. D. & Silver, P.G. (2009). Shear wave splitting and Mantle anisotropy: Interpretations, and new directions. Surveys in Geophysics 30, 407–461.

Long, M. D. & Becker, T. W. (2010). Mantle dynamics and seismic anisotropy. Earth and Planetary Science Letters 297, 341–354.

Mainprice, D., Barruol, G. & Ben Ismaïl, W. (2000). The seismic anisotropy of the Earth's mantle: from single crystal to polycrystal. In: S.I. Karato, A. Forte, R.C. Liebermann, G. Masters and L. Stixrude (Editors), Earth's deep interior: Mineral Physics and Tomography from the atomic to the global scale. Geophysical Monograph. AGU, Washington, D.C., 237-264.

Mainprice, D. & Silver, P.G. (1993). Interpretation of SKS waves using samples from the subcontinental lithosphere. Phys. Earth Planet. Inter. 78, 257–280.

Meffre, S., Berry, R. F. & Hall, M. (2000). Cambrian metamorphic complexes in Tasmania: tectonic implications. Australian Journal of Earth Sciences 47, 971–985.

Milligan, P. R., Franklin, R., Minty, B. R. S., Richardson, L. M. & Percival, P. J. (2010). Magnetic anomaly map of Australia (Fifth edition), 1:15 000 000 scale, Geoscience Australia, Canberra.

Moore, D. H., Betts, P. G. & Hall, M. (2013). Towards understanding the early Gondwana margin in southeastern Australia. Gondwana Research 23, 1581-1598.

Moore, D. H., Betts, P. G. & Hall, M. (2015). Fragmented Tasmania: the transition from Rodinia to Gondwana. Australian Journal of Earth Sciences 62, 1-35.

Moresi, L., Betts, P. G., Miller, M. S. & Cayley, R. A. (2014). Dynamics of continental accretion. Nature 508, 245 - 248.

Morgan, W. J. (1971). Convection plumes in the lower mantle. Nature 230, 42 - 43.

Nicolas, A. & Christensen N. I. (1987). Formation of anisotropy in upper mantle peridotite. Geodyn. Ser. 16, 111-123.

Ozalaybey, S. & Chen, W.-P. (1999). Frequency-dependent analysis of SKS/SKKS waveforms observed in Australia: evidence for null birefringence, Phys. Earth Planet. Inter. 114, 197 – 210.

Pilia, S., Rawlinson, N., Green, N., Reading, A. M., Cayley, R., Pryer, L., Arroucau, P. & Duffet, M. (2015a).

Linking mainland Australia and Tasmania using ambient seismic noise tomography: Implications for the tectonic evolution of the east Gondawana margin. Gondwana Research 28, 1212-1227.

Pilia, S., Rawlinson, N., Cayley, R.A., Musgrave, R., Reading, A.M., Direen, N.G. & Young, M.K. (2015b). Evidence of micro-continent entrainment during crustal accretion. Sci. Rep., 5. http://dx.doi.org/10.1038/srep/08218.

Pilia, S., Arroucau, P., Rawlinson, N., Reading, A.M. & Cayley, R.A. (2016). Inherited crustal deformation along the East Gondwana margin revealed by seismic anisotropy tomography. Geophysical Research Letters 43 (23), 12,082-12,090. ISSN 0094–8276, DOI: 10.1002/2016GL071201.

Rawlinson, N., Reading, A.M. & Kennett, B.L.N. (2006). Lithospheric structure of Tasmania from a novel form of teleseismic tomography. Journal of Geophysical Research 111, http://dx.doi.org/10.1029/2005JB003803.

Rawlinson N. & Urvoy M. (2006). Simultaneous inversion of active and passive source datasets for 3-D seismic structure with application to Tasmania. Geophysical Research Letters 33, DOI:10.1029/2006GL028105.

Rawlinson, N. & Kennett, B. L. N. (2008). Teleseismic tomography of the upper mantle beneath the southern Lachlan Orogen. Physics of the Earth and Planetary Interiors 167, 84–97.

Rawlinson, N. & Fishwick, S. (2011). Seismic structure of the southeast Australian lithosphere from surface and body wave tomography. Tectonophysics, DOI:10.1016/j.tecto.2011.11.016.

Rawlinson, N., Kennett, B. L. N., Salmon, M. & Glen, R. A. (2015). Origin of lateral heterogeneities in the upper mantle beneath Southeast Australia from seismic tomography. In: Khan, A., Deschamps, F. (Eds.), The Earth's Heterogeneous Mantle: A Geophysical, Geodynamical and Geochemical Perspective, Springer Geophysics. Springer, 47–78.

Rawlinson, N., Pilia, S., Young, M. Salmon, M. & Yang, Y. (2016). Crust and upper mantle structure beneath southeast Australia from ambient noise and teleseismic tomography. Tectonophysics 689, 143-156. http://dx.doi.org/10.1016/j.tecto.2015.11.034.

Rawlinson, N., Davies, D. R. & Pilia S. (2017). The mechanisms underpinning Cenozoic intraplate volcanism in eastern Australia: Insights from seismic tomography and geodynamic modeling. Geophys. Res. Lett. 44, 9681–9690, DOI:10.1002/2017GL074911.

Reed, A. R., Calver, C. & Bottrill, R.S. (2002). Palaeozoic suturing of eastern and western Tasmania in the west Tamar region: implications for the tectonic evolution of southeast Australia. Australian Journal of Earth Sciences 49, 809–830.

Reed, A. R. (2001). Pre-Tabberabberan deformation in eastern Tasmania: a southern extension of the Benambran Orogeny. Australian Journal of Earth Sciences 48, 785–796. http://dx.doi.org/10.1046/j.1440-0952.2001.00900.x.

Rosenbaum, G., Pengfei, L. & Rubatto, D. (2012). The contorted New England Orogen (eastern Australia): new evidence from U–Pb geochronology of early Permian granitoids. Tectonics 31. http://dx.doi.org/10.1029/2011TC002960.

Rümpker, G. & Silver, P.G. (2000). Calculating splitting parameters for plume-type anisotropic structures of the upper mantle, Geophys. J. Int. 143, 507–520.

Savage, M. (1999). Seismic anisotropy and mantle deformation: What have we learned from shear wave splitting, Rev. Geophys. 37, 65–106, DOI:10.1029/98RG02075.

Seymour, D. B., Green, G. R. & Calver, C. R. (2007). The Geology and Mineral Deposits of Tasmania: a summary. Geological Survey Bulletin 72, Second Edition, ISBN 0 7246 4017 7.

Siégel, C., Bryan, S. E., Allen, C. M., Purdey, D. J., Cross, A. J., Uysal, I. T. & Gust, D. A. (2018). Crustal and thermal structure of the Thomson Orogen: constraints from the geochemistry, zircon U-Pb age, and Hf and O isotopes of subsurface granitic rocks. Australian Journal of Earth Sciences, DOI: 10.1080/08120099.2018.1447998.

Silver, P.G. & Chan, W.W. (1988). Implications for continental structure and evolution from seismic anisotropy, Nature 335, 34–39.

Silver, P.G. & Chan, W.W. (1991). Shear wave splitting and subcontinental mantle deformation. J. Geophys. Res. 96, 16,429–16,454.

Silver, P.G. & Savage, M.K. (1994). The interpretation of shear-wave splitting parameters in the presence of two anisotropic layers. Geophys. J. Int. 119, 494–963.

Silver, P.G. (1996). Seismic anisotropy beneath the continents: probing the depths of geology. Annu. Rev. Earth Planet. Sci. 24, 385–432.

Simons, F.J. & Van der Hilst, R.D. (2003). Seismic and mechanical anisotropy and the past and present deformation of the Australian lithosphere. Earth Planet. Sci. Lett. 211, 271 – 286.

Sleep, N., Ebinger, C. & Kendall, J. -M. (2002). Deflection of mantle plume material by cratonic keels. Geol. Soc. London Spec. Publ. 199, 135–150, DOI:10.1144/GSL.SP.2002.199.01.08.

Spampinato, G. P. T., Ailleres, L., Betts, P. G. & Armit, R. J. (2015). Crustal architecture of the Thomson Orogen in Queensland inferred from potential field forward modelling. Australian Journal of Earth Sciences 62:5, 581-603, DOI: 10.1080/08120099.2015.1063546.

Stotz, I.L., Iaffaldano, G. & Davies, D.R. (2018). Pressure-Driven Poiseuille Flow: A Major Component of the Torque-Balance Governing Pacific Plate Motion. Geophys. Res. Lett. 45(1), 117-125, DOI:10.1002/2017GL075697.

Teanby, N., Kendall, J. -M. & Van der Baan, M. (2004). Automation of shear-wave splitting measurements using cluster analysis. Bull. Seismol. Soc. Am. 94, 453–463, DOI:10.1785/0120030123.

Tommasi, A. (1998). Forward modeling of the development of seismic anisotropy in the upper mantle. Earth Planet. Sci. Lett. 160, 1-13.

Turner, N., Black, L. P. & Kamperman, M. (1998). Dating of Neoproterozoic and Cambrian orogenesis in Tasmania. Aust. J. Earth. Sci. 45, 789–806.

van der Beek, P. A., Braun, J. & Lambeck, K. (1999). Post-Paleozoic uplift history of southeastern Australia revisited: Results from a process-based model of landscape evolution, Aust. J. Earth Sci. 46, 157-172.

Vauchez, A. & Nicolas, A. (1991). Mountain building: Strike-parallel motion and mantle anisotropy. Tectonophysics 185, 183–201, DOI: 10.1016/0040-1951(91) 90443-V.

Vinnik, L. P., Kosarev, G. L. & Makeyeva, L. I. (1984). Anisotropiya litospery po nalblyudeniyam vol SKS and SKKS, Dokl. Akad. Nauk USSR 278, 1335-1339.

Vinnik, L., Farra, V. & Romanowicz, B. (1989). Azimuthal anisotropy in the Earth from observations of SKS at Geoscope and NARS broadband stations, Bull. Seismol. Soc. Am. 79, 1542–1558.

Vinnik, L., Makeyeva, L., Milev, A. & Usenko, A. Y. (1992). Global patterns of azimuthal anisotropy and deformations in the continental mantle, Geophys. J. Int. 111, 433–447.

Walker, K. T., Nyblade, A.A., Klemperer, S.L., Bokelmann, G.H.R. & Owens, T.J. (2004). On the relationship between extension and anisotropy: constraints from shear wave splitting across the East African plateau, J. geophys. Res. 109, 1–21.

Walker, K. T., Bokelmann, G.H. R., Klemperer, S.L. & Bock, G. (2005). Shear-wave splitting around the Eifel hotspot: evidence for a mantle up- welling, Geophys. J. Int. 163, 962–980.

Williams, E. (1989). Summary and synthesis, in Geology and Mineral Resources of Tasmania, edited by C. F. Burrett and E. L. Martin, Spec. Publ. Geol. Soc. Aust. 15, 468 – 499.

Wilson, J. T. (1963). A possible origin of Hawaiian Islands, Can. J. Phys. 41, 863-870.

Zhang, S. & Karato, S. (1995). Lattice preferred orientation of olivine aggregates deformed in simple shear, Nature 375, 774 – 777.

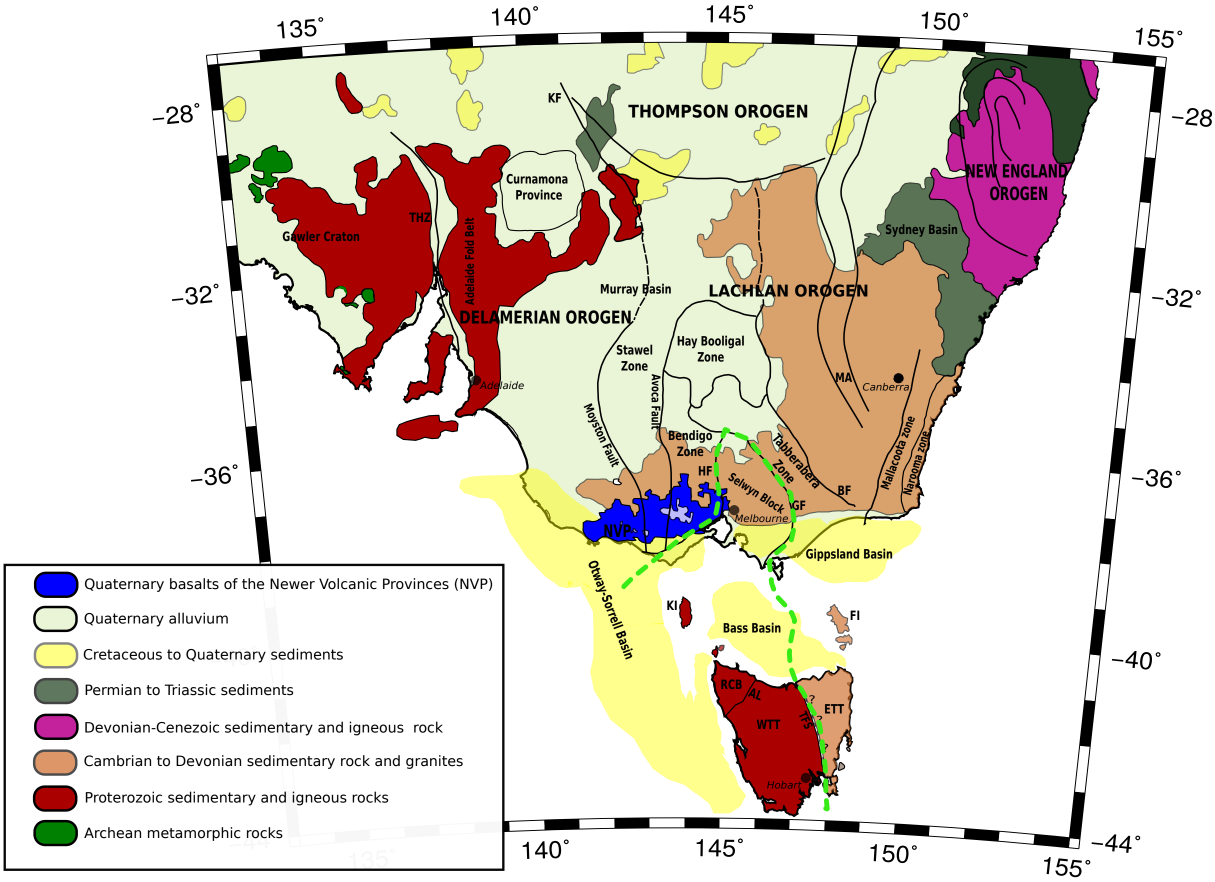

Fig. 1: Simplified geological map of southeastern Australia showing observed and inferred geological boundaries and main tectonic features mentioned in the text. Thick black lines show locations of structural boundaries. Thick green dashed line denotes the boundary of VanDieland. KF = Koonenberry Fault; HF = Heathcote Fault; GF = Governor Fault; BF = Bootheragandra Fault; THZ = Torrens Hinge Zone; NVP = Newer Volcanic Province; MA = Macquarie Arc; KI = King Island and FI = Flinders Island in Bass Strait; WTT = Western Tasmania Terrane; ETT = Eastern Tasmania Terrane; AL = Arthur Lineament; TFS = Tamar Fracture System and RCB = Rocky Cape Block.

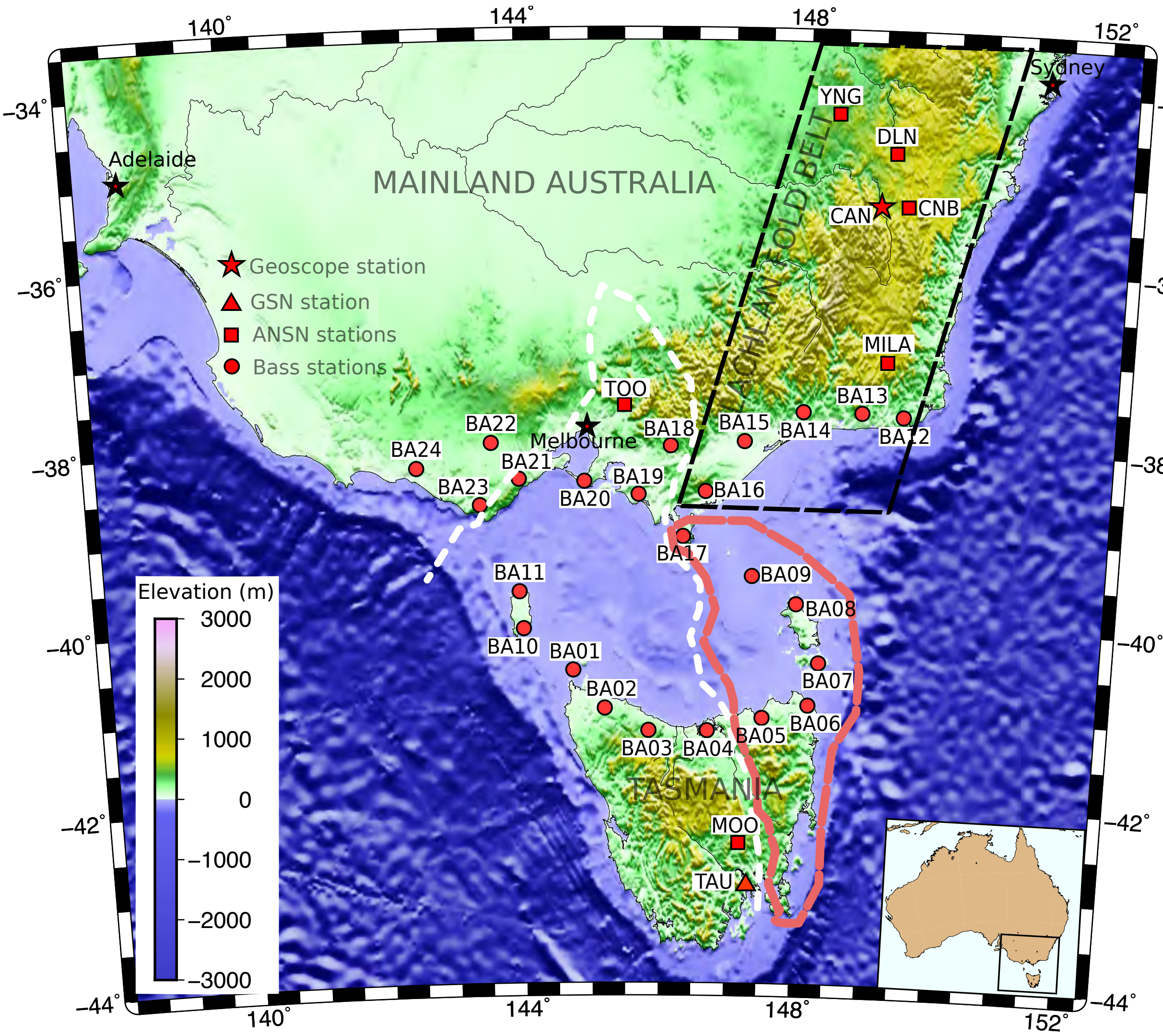

Fig. 2: Topographic/bathymetric map of the study area showing main tectonic blocks and locations of the 32 broadband instruments mentioned in the text. Thick white dashed line denotes the boundary of VanDieland. Thick red dashed line outlines the boundary of East Tasmania terranne and Furneaux Islands. Thick black dashed line highlights part of the Lachlan Fold Belt.

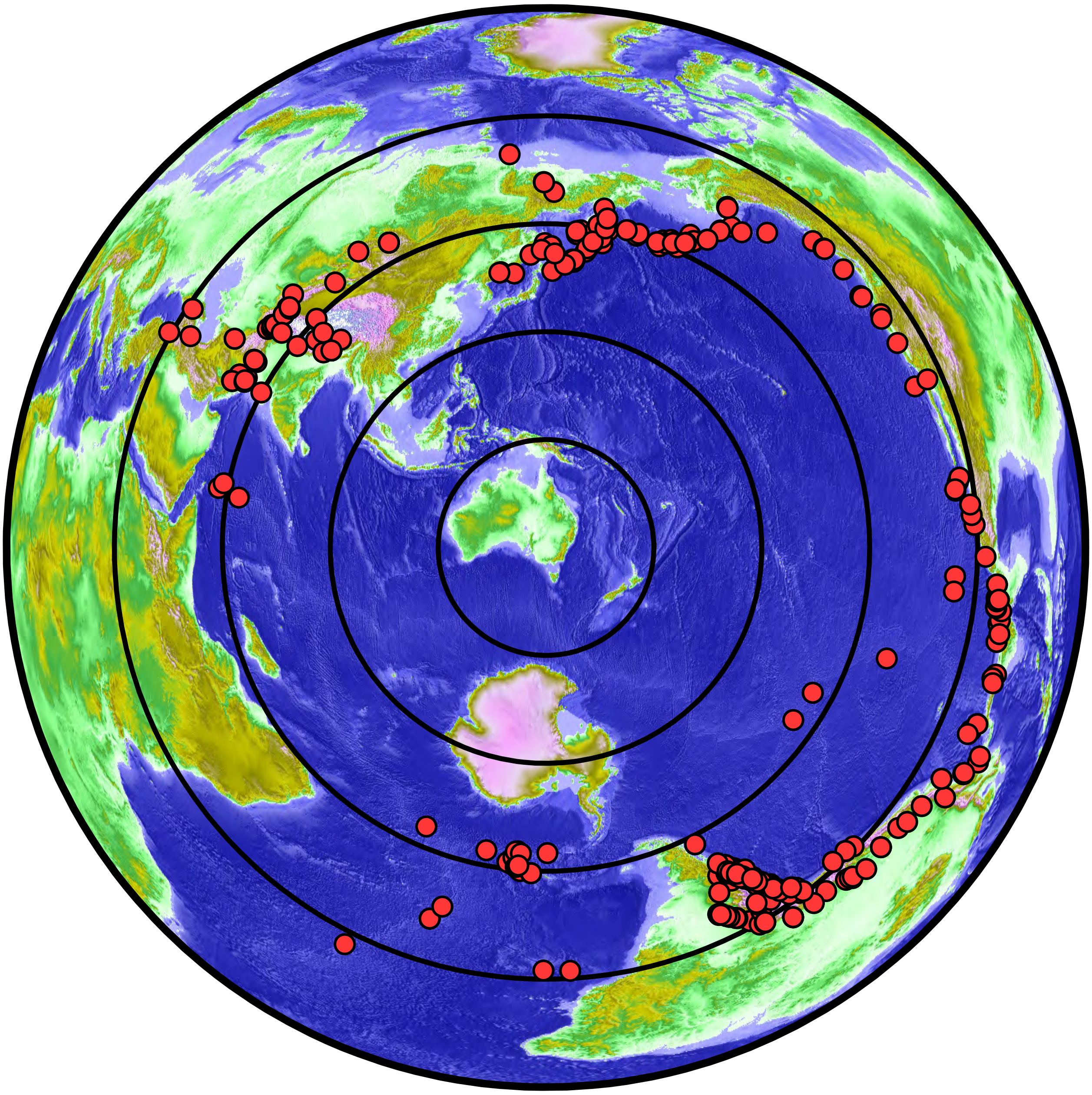

Fig. 3: Distribution of teleseismic events used for this study. Concentric circles are plotted at 30° intervals from the centre of Bass Strait.

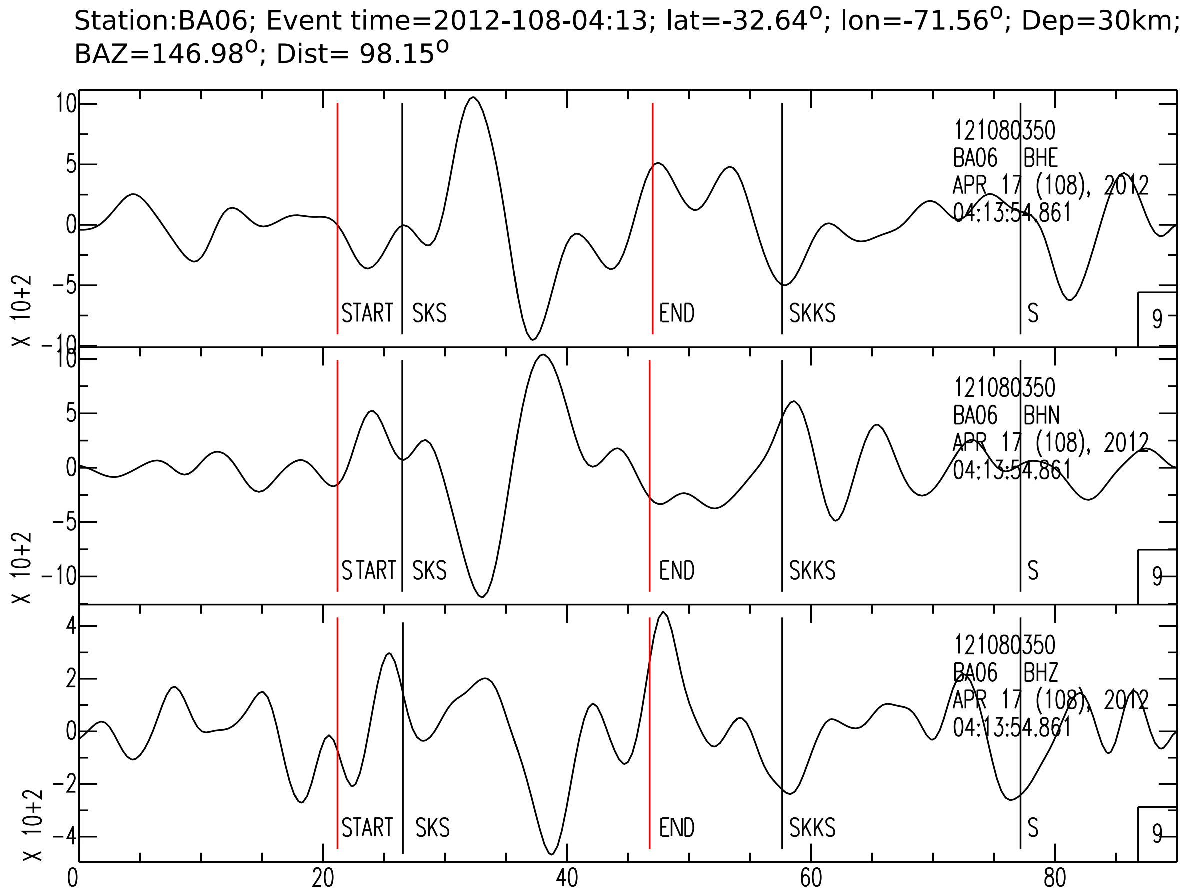

Fig. 4: Example of a filtered seismogram at station BA06, with the expected arrival times for SKS and SKKS from the ak135 earth model shown. Red vertical lines represent the time window chosen for analysis (marked START and END).

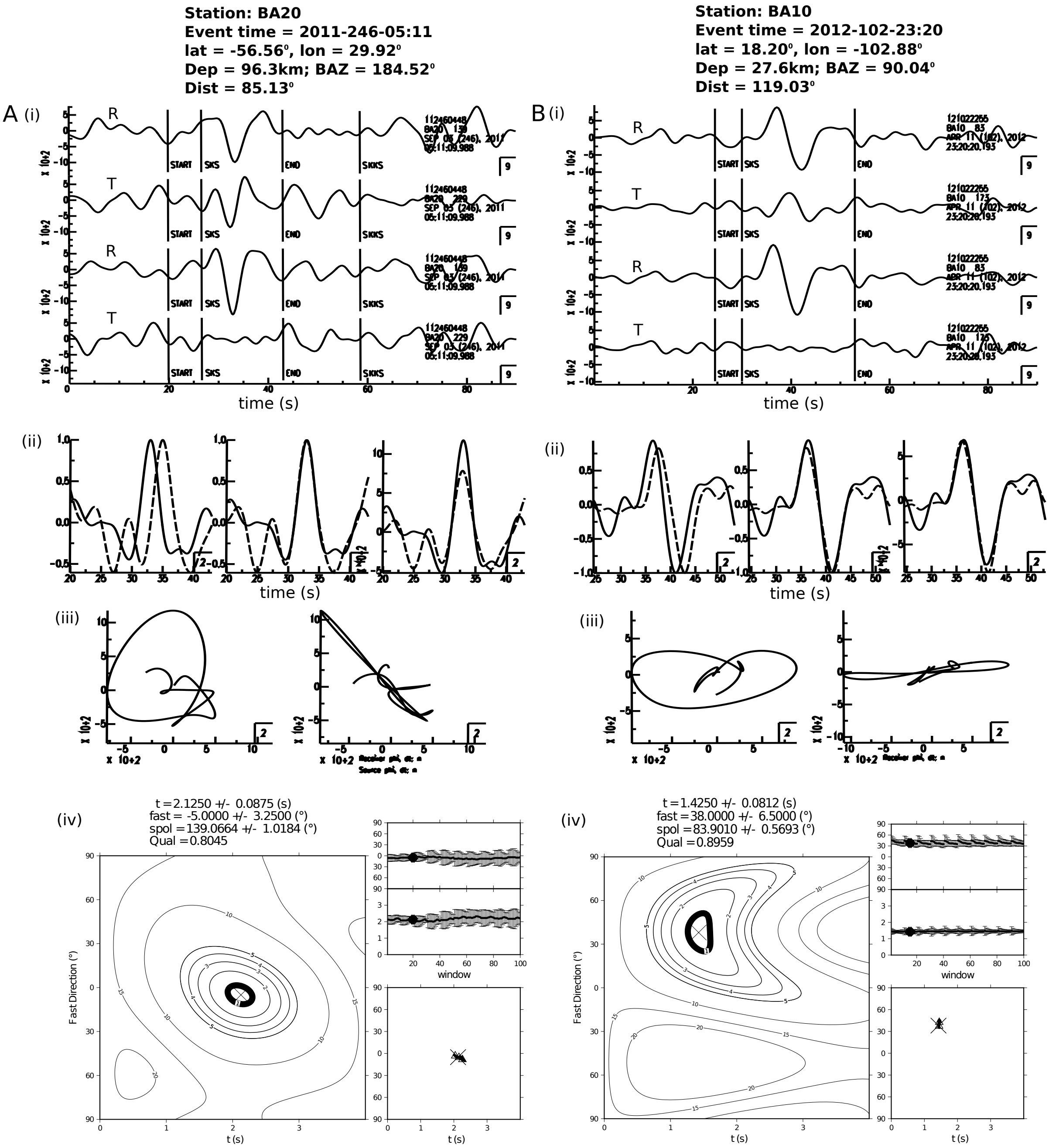

Fig. 5: Examples of shear wave splitting analyses for stations BA20 and BA10 which produce high quality split measurements. In each case (BA20(A) and BA10(B)): (i) radial and tangential components before (top) and after (bottom) correction by the splitting analysis; tangential SKS energy is minimized, (ii) windowed waveforms (dashed line: fast, solid line: slow) before and after correction applied; plot 2 is normalized and plot 3 shows the corrected waves with their relative amplitudes preserved, (iii) particle motion before and after correction, showing the change from elliptical to linearized motion, and (iv) grid search and cluster analysis outputs. The main graphic shows the final grid search results for ϕ and δt; the two smaller plots show individual measurements of ϕ and δt for the 100 windows used in the analysis.

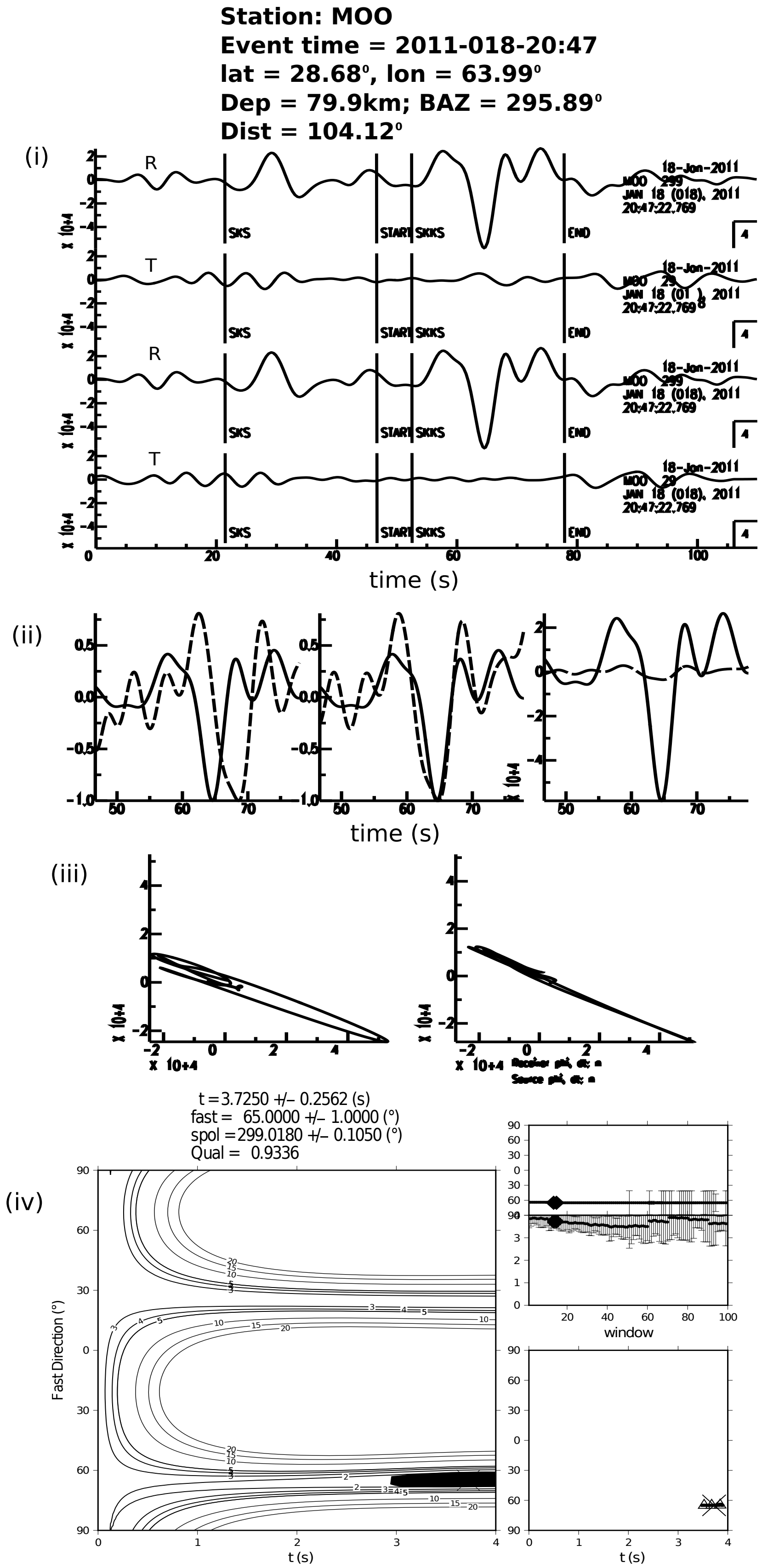

Fig. 6: A high-quality null. In this case, there is no signal on the tangential-component waveform, and the particle motion is linear both before and after analysis.

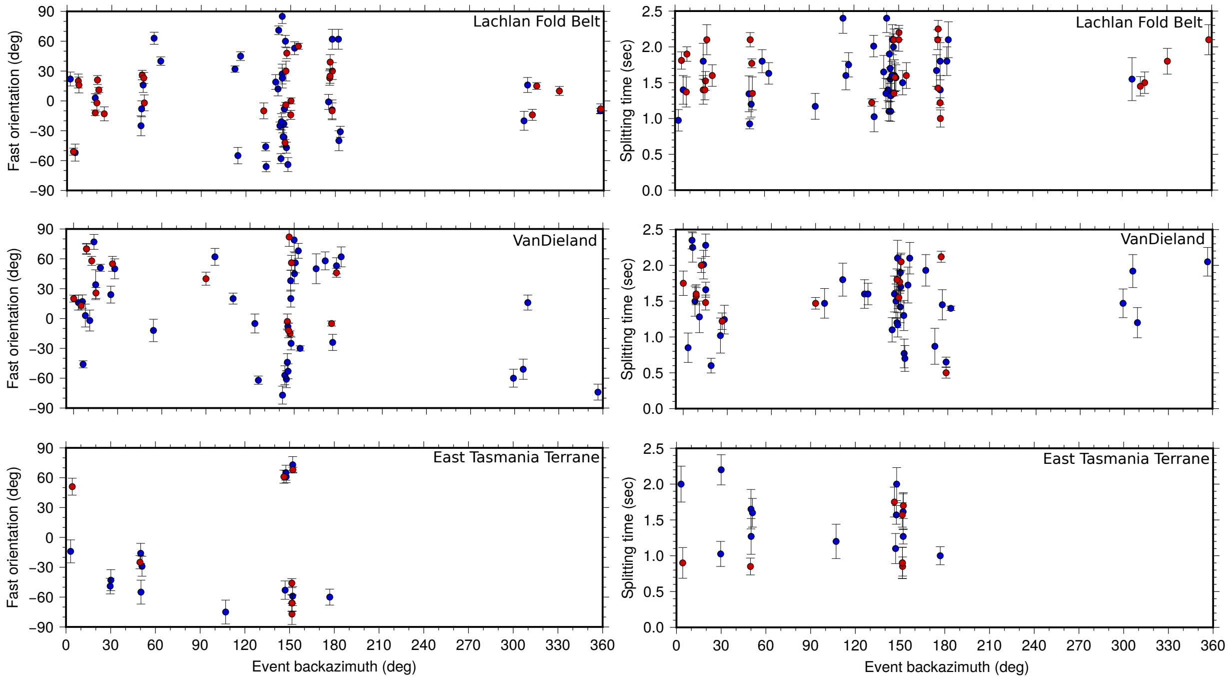

Fig. 7: Examples of the back azimuthal coverage of splitting results for the three tectonic blocks discussed in the text: Lachlan Fold Belt, VanDieland and East Tasmania Terrane + Furneaux Island. For each tectonic block, the left graph shows fast orientations and the right graph shows delay time; red represents good measurements, and blue represents fair measurements.

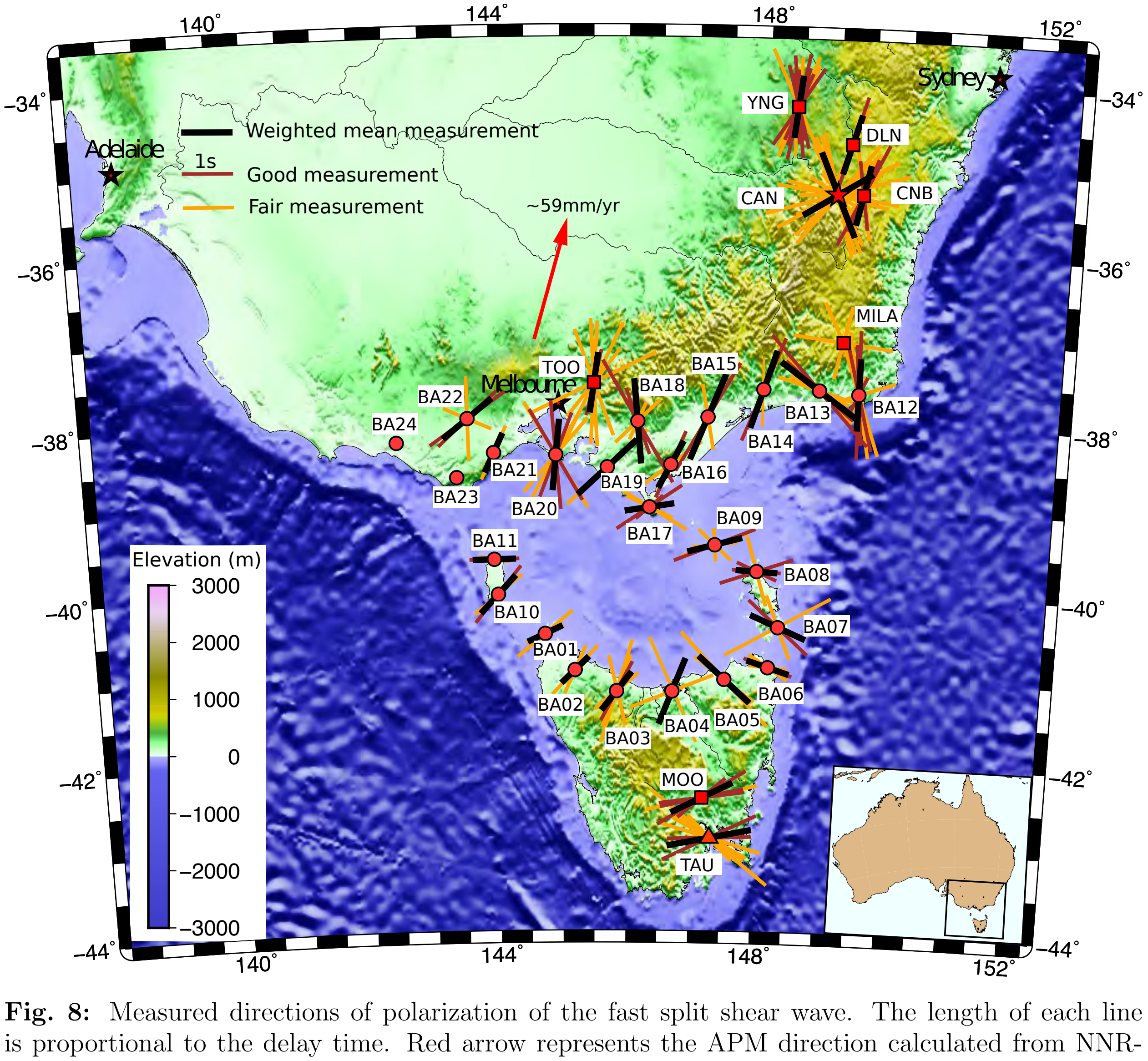

Fig. 8: Measured directions of polarization of the fast split shear wave. The length of each line is proportional to the delay time. Red arrow represents the APM direction calculated from NNR-MORVEL56 (Argus et al., 2011).

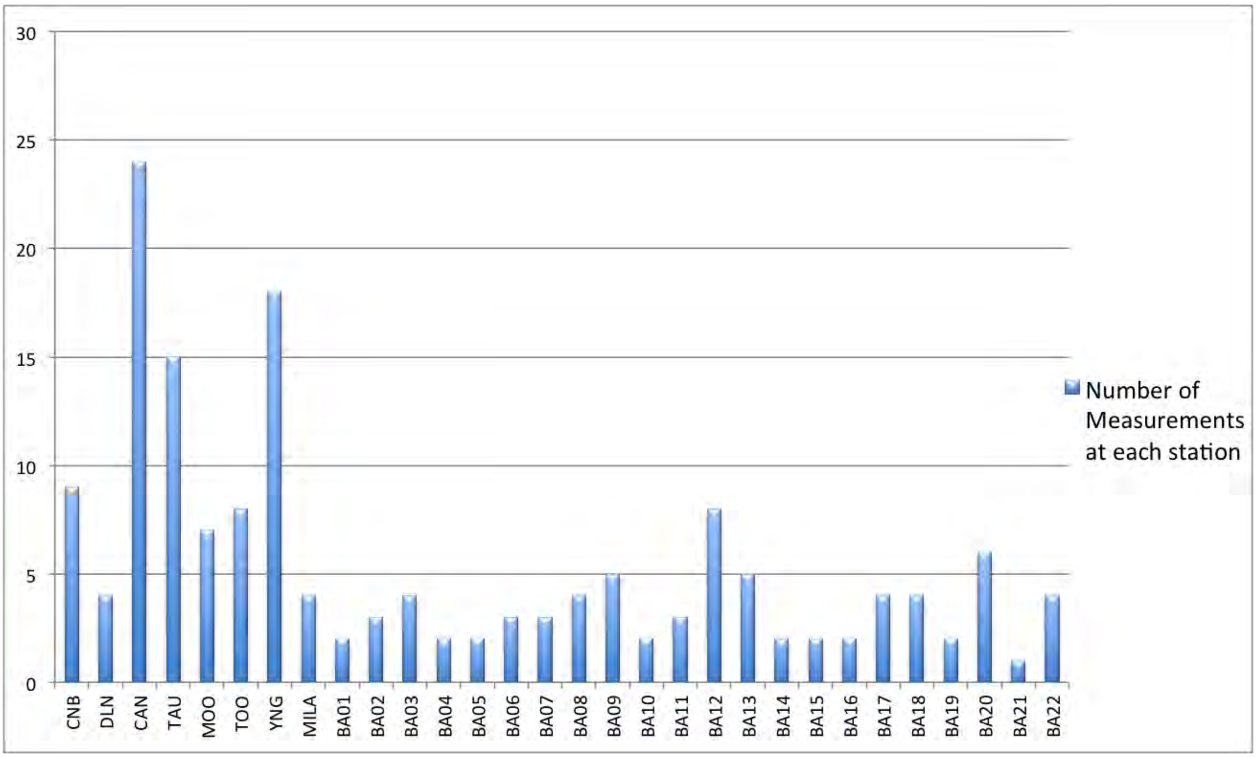

Fig. 9: A bar chart illustrating the number of measurements at individual stations.

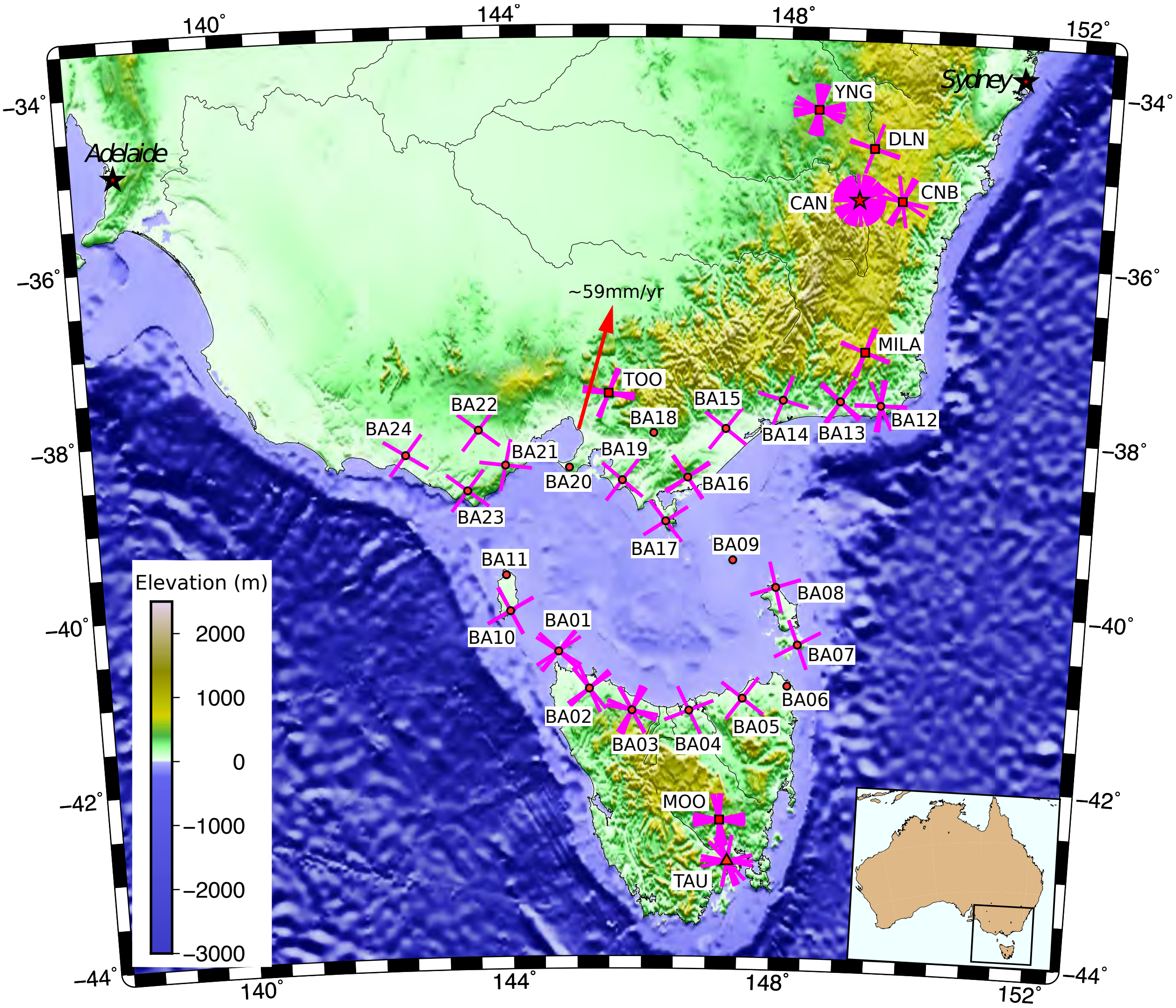

Fig. 10: Plot of null measurements for each station. The crosses denote absence of splitting: each branch is either parallel or perpendicular to a possible direction of anisotropy. Red arrow represents the APM direction calculated from NNR-MORVEL56 (Argus et al., 2011).

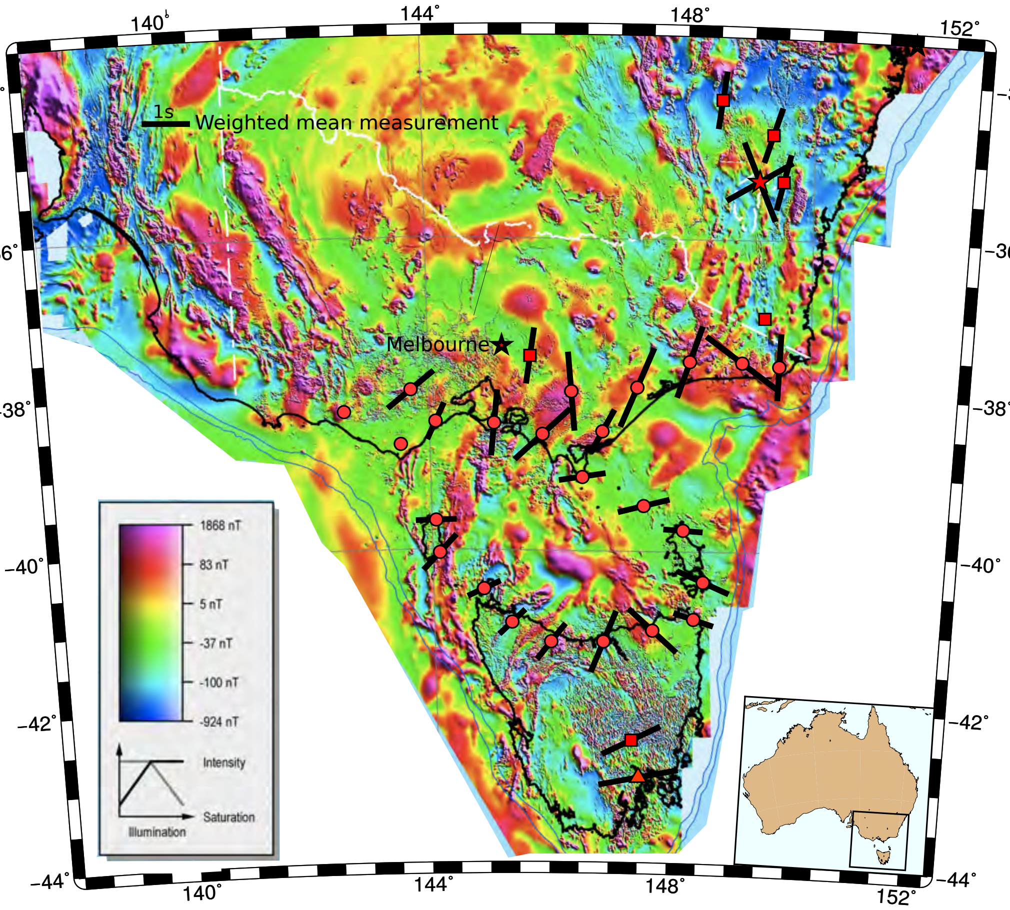

Fig. 11: Measured directions of polarization of the fast split shear wave superimposed on a magnetic anomaly map (modified from Milligan et al., 2010). The length of each line is proportional to the delay time.

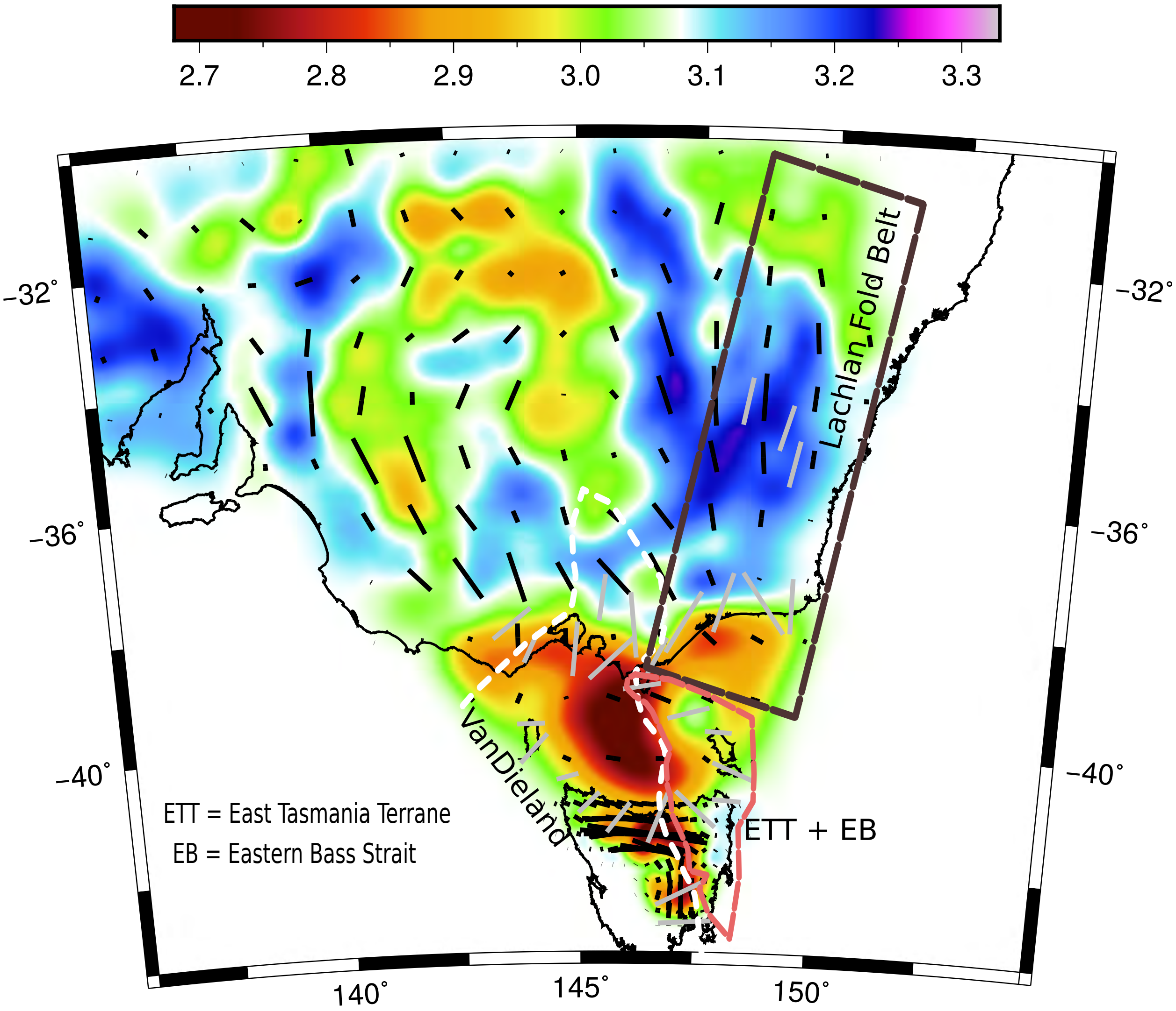

Fig. 12: Comparison of the new weighted mean SKS/SKKS splits (grey bars) superimposed on 5 second period Rayleigh wave phase anisotropy variations in the crust (black bars) (Pilia et al., 2016). For the Rayleigh wave phase anisotropy (black bars), the length of the bars is proportional to the magnitude of anisotropy, and the direction is aligned with the fast axis of anisotropy. The SKS/SKKS splits (grey bars) are scaled to 75% of the delay time magnitude for ease of comparison. The background colour represents the isotropic component of the 2D phase velocity map.

Table. 1: Weighted mean SKS/SKKS splitting parameters for each station. Quality assignments are given as: g = good; f = fair; and N = Null

<table>
<tr><th rowspan="2">Station</th><th rowspan="2">Lat. (°)</th><th rowspan="2">Long.(°)</th><th rowspan="2">Network</th><th rowspan="2">Total</th><th rowspan="2">Measurement categorisation</th><th colspan="2">ϕ (weighted mean)</th><th colspan="2">δt (weighted mean)</th></tr>
<tr><th>Upper (°)</th><th>Lower(°)</th><th>Upper(s)</th><th>Lower(s)</th></tr>
<tr><td>YNG</td><td>-34.298</td><td>148.396</td><td>ANSN</td><td>40</td><td>11g + 7f + 21N</td><td colspan="2">7 ± 3</td><td colspan="2">1.36 ± 0.07</td></tr>
<tr><td>CNB</td><td>-35.315</td><td>149.363</td><td>ANSN</td><td>19</td><td>3g + 6f + 10N</td><td colspan="2">13 ± 3</td><td colspan="2">1.30 ± 0.14</td></tr>
<tr><td>CAN</td><td>-35.319</td><td>148.996</td><td>GEOSCOPE</td><td>65</td><td>0g + 24f + 41N</td><td>58 ± 3</td><td>-23 ± 2</td><td>1.58 ± 0.15</td><td>1.78 ± 0.18</td></tr>
<tr><td>TAU</td><td>-42.909</td><td>147.320</td><td>GSN</td><td>36</td><td>3g + 12f + 21N</td><td colspan="2">81 ± 9</td><td colspan="2">1.34 ± 0.11</td></tr>
<tr><td>MOO</td><td>-42.442</td><td>147.190</td><td>ANSN</td><td>23</td><td>5g + 2f + 16N</td><td colspan="2">63 ± 3</td><td colspan="2">1.33 ± 0.06</td></tr>
<tr><td>TOO</td><td>-37.571</td><td>145.491</td><td>ANSN</td><td>18</td><td>1g +7f + 10N</td><td colspan="2">08 ± 3</td><td colspan="2">1.19 ± 0.16</td></tr>
<tr><td>DLN</td><td>-34.723</td><td>149.179</td><td>ANSN</td><td>9</td><td>1g +3f + 5N</td><td colspan="2">16 ± 2</td><td colspan="2">1.22 ± 0.13</td></tr>
<tr><td>BA01</td><td>-40.523</td><td>144.741</td><td>BASS</td><td>8</td><td>0g + 2f + 6N</td><td colspan="2">65 ± 4</td><td colspan="2">0.66 ± 0.10</td></tr>
<tr><td>BA02</td><td>-40.950</td><td>145.200</td><td>BASS</td><td>7</td><td>1g + 2f + 4N</td><td colspan="2">46 ± 2</td><td colspan="2">0.75 ± 0.07</td></tr>
<tr><td>BA03</td><td>-41.199</td><td>145.841</td><td>BASS</td><td>17</td><td>1g + 3f + 13N</td><td colspan="2">38 ± 3</td><td colspan="2">0.95 ± 0.04</td></tr>
<tr><td>BA04</td><td>-41.196</td><td>146.704</td><td>BASS</td><td>4</td><td>0g +2f + 2N</td><td colspan="2">21 ± 4</td><td colspan="2">1.39 ± 0.19</td></tr>
<tr><td>BA05</td><td>-41.050</td><td>147.506</td><td>BASS</td><td>5</td><td>0g +2f + 3N</td><td colspan="2">-48 ± 3</td><td colspan="2">1.35 ± 0.15</td></tr>
<tr><td>BA06</td><td>-40.900</td><td>148.176</td><td>BASS</td><td>3</td><td>1g + 3f + 0N</td><td colspan="2">-86 ± 3</td><td colspan="2">0.73 ± 0.11</td></tr>
<tr><td>BA07</td><td>-40.426</td><td>148.314</td><td>BASS</td><td>5</td><td>1g + 2f + 2N</td><td colspan="2">-67 ± 4</td><td colspan="2">1.17 ± 0.07</td></tr>
<tr><td>BA08</td><td>-39.774</td><td>147.966</td><td>BASS</td><td>7</td><td>3g + 1f + 3N</td><td colspan="2">-87 ± 2</td><td colspan="2">0.68 ± 0.12</td></tr>
<tr><td>BA09</td><td>-39.470</td><td>147.323</td><td>BASS</td><td>5</td><td>1g +4 f + 0N</td><td colspan="2">75 ± 3</td><td colspan="2">1.10 ± 0.03</td></tr>
<tr><td>BA10</td><td>-40.056</td><td>144.030</td><td>BASS</td><td>7</td><td>1g + 1f + 5N</td><td colspan="2">43 ± 1</td><td colspan="2">1.03 ± 0.06</td></tr>
<tr><td>BA11</td><td>-39.644</td><td>143.977</td><td>BASS</td><td>3</td><td>1g + 2f + 0N</td><td colspan="2">89 ± 5</td><td colspan="2">0.71 ± 0.13</td></tr>
<tr><td>BA12</td><td>-37.662</td><td>149.412</td><td>BASS</td><td>14</td><td>4g + 4f + 6N</td><td colspan="2">1 ± 2</td><td colspan="2">1.41 ± 0.18</td></tr>
<tr><td>BA13</td><td>-37.628</td><td>148.828</td><td>BASS</td><td>9</td><td>2g + 3f + 4N</td><td colspan="2">-54 ± 2</td><td colspan="2">1.87 ± 0.05</td></tr>
<tr><td>BA14</td><td>-37.630</td><td>148.004</td><td>BASS</td><td>4</td><td>1g + 1f + 3N</td><td colspan="2">18 ± 4</td><td colspan="2">1.59 ± 0.14</td></tr>
<tr><td>BA15</td><td>-37.967</td><td>147.186</td><td>BASS</td><td>4</td><td>1g + 1f + 2N</td><td colspan="2">22 ± 3</td><td colspan="2">1.79 ± 0.17</td></tr>
<tr><td>BA16</td><td>-38.531</td><td>146.643</td><td>BASS</td><td>7</td><td>1g + 1f + 6N</td><td colspan="2">28 ± 2</td><td colspan="2">1.04 ± 0.12</td></tr>
<tr><td>BA17</td><td>-39.035</td><td>146.327</td><td>BASS</td><td>6</td><td>2g + 2f + 2N</td><td colspan="2">81 ± 6</td><td colspan="2">0.98± 0.13</td></tr>
<tr><td>BA18</td><td>-38.025</td><td>146.143</td><td>BASS</td><td>4</td><td>2g + 2f + 0N</td><td colspan="2">-5 ± 4</td><td colspan="2">1.68 ± 0.04</td></tr>
<tr><td>BA19</td><td>-38.566</td><td>145.691</td><td>BASS</td><td>3</td><td>0g + 1f + 4N</td><td colspan="2">47 ± 9</td><td colspan="2">1.59 ± 0.18</td></tr>
<tr><td>BA20</td><td>-38.420</td><td>144.920</td><td>BASS</td><td>6</td><td>3g + 3f + 0N</td><td colspan="2">6 ± 2</td><td colspan="2">1.40 ± 0.09</td></tr>
<tr><td>BA21</td><td>-38.391</td><td>143.990</td><td>BASS</td><td>4</td><td>0g +1f + 3N</td><td colspan="2">25 ± 9</td><td colspan="2">1.15 ± 0.21</td></tr>
<tr><td>BA22</td><td>-37.986</td><td>143.605</td><td>BASS</td><td>6</td><td>2g + 2f + 2N</td><td colspan="2">51 ± 3</td><td colspan="2">1.24 ± 0.16</td></tr>
</table>

Supporting Information for “Insights into the structure and dynamics of the upper mantle beneath Bass Strait, southeast Australia, using shear wave splitting”

M. Bello*[1,2], D.G. Cornwell[1], N. Rawlinson[3] and A. M. Reading[4]

Corresponding author: mbazare13@yahoo.com; r02mb15@abdn.ac.uk

[1]School of Geosciences, University of Aberdeen, Aberdeen, UK

[2]Department of Physics, Abubakar Tafawa Balewa University, Bauchi, Nigeria

[3]Department of Earth Sciences-Bullard Labs, University of Cambridge, Cambridge, UK

[4]School of Natural Sciences (Physics), University of Tasmania, Tasmania, Australia

Contents of this file

Introduction. The supplementary material consists of tables which provide all of the individual shear-wave splitting measurements used in the analysis. The earthquakes mentioned in the tables are labelled according to the origin time of the event, in the format yyjjjhhmmss i.e. year, Julian day, hour, minute, second. The phase used in the analysis is the SKS core phase unless otherwise stated (e.g. SKKS phase). The event back-azimuth is given in the second column and the splitting parameters in subsequent columns. Since nulls have a 90° ambiguity in addition to the inherent 180° ambiguity of orientation, the null results are given here in the same quadrant as the event back-azimuth. Delay times are undefined for nulls.

Table S1. Splitting measurements for stations CNB, DLN, CAN (Permanent stations)

Station	Event	Back-azimuth (°)	Fast-direction (°)	Splitting time (s)	Result type
CNB	07227202213	20	21±8	1.52±0.08	split
CNB	09072272340	130	16±10	1.53±0.16	split
CNB	08009082648	310	26±16	2.23±0.03	split
CNB	08119155751	183	282	n/a	null
CNB	08303113241	300	24	n/a	null
CNB	09317030558	139	23	n/a	null
CNB	10064114707	147	8±6	1.36±0.10	split
CNB	08054155719	184	23	n/a	null
CNB	08279155250	310	-12±8	0.73±0.13	split
CNB	09106145706	182	351	n/a	null
CNB	10075022158	146	32	n/a	null
CNB	10059112535	25	37±9	1.35±0.23	split
CNB	11261124049	309	-9±5	1.07±0.46	split
CNB	11018202325 (SKKS)	296	22	n/a	null
CNB	12176031501	8	18±11	1.47±0.16	split
CNB	11245134710	150	26	n/a	null
CNB	14032035845	182	-10±3	1.22±0.36	split
CNB	15264174000	145	302	n/a	null
CNB	15351194953	92	280	n/a	null
DLN	08187021206	2	23±8	1.50±0.20	split
DLN	15033104948	149	21±6	1.09±0.31	split
DLN	15299090942	306	19	n/a	null
DLN	15132070519	308	74	n/a	null
DLN	15341075005	304	310	n/a	null
DLN	16041003305	144	22±6	1.11±0.18	split
DLN	16080225020	8	16±8	1.21±0.09	split
DLN	16101102858	306	71	n/a	null
DLN	17095060912	301	285	n/a	null
CAN	05080122853	144	77±13	1.42±0.12	split
CAN	05080212273	148	88±11	1.55±0.24	split
CAN	08238132201	309	39±8	2.53±0.16	split
CAN	08304151540	105	291	n/a	null
CAN	09317030558	139	286	n/a	null
CAN	10064114707	147	88	n/a	null
CAN	10070143945	146	60±10	2.31±0.14	split
CAN	10113100306	148	59±9	1.30±0.17	split
CAN	11001095658	149	-28±3	2.20±0.46	split
CAN	10199055645	24	277	n/a	null
CAN	10216125825	20	21	n/a	null
CAN	11002202018	148	305	n/a	null
CAN	11018202325	296	298	n/a	null
CAN	11200193543	310	18±11	2.05±0.21	split
CAN	11236174611	127	-38±12	0.95±0.06	split
CAN	11341222307	143	40±10	1.97±0.25	split
CAN	12135100039	139	-78±12	0.80±0.21	split
CAN	11045034009	146	296	n/a	null
CAN	11207174421	75	355	n/a	null
CAN	11245105555	23	22	n/a	null
CAN	11245134710	150	340	n/a	null

Table S2. Splitting measurements for stations CAN (cont'd) (Permanent stations)

Station	Event	Back-azimuth (°)	Fast-direction (°)	Splitting time (s)	Result type
CAN	12176031502	8	74±17	2.01±0.23	split
CAN	12298004533	103	31±12	1.32±0.08	split
CAN	12302185420	40	-82±16	2.12±0.18	split
CAN	14043091948	35	-34±10	1.12±0.21	split
CAN	11301185430	131	60	n/a	null
CAN	11326184816	141	319	n/a	null
CAN	12023160453	147	338	n/a	null
CAN	12057061719	330	333	n/a	null
CAN	14057211340	22	78±12	0.85±0.23	split
CAN	15264174000	145	-23±11	2.41±0.20	split
CAN	12085223706	147	31	n/a	null
CAN	12249144207	103	63±9	1.80±0.17	split
CAN	11222416313	118	293	n/a	null
CAN	15351194953	92	38±12	0.97±0.02	split
CAN	16139075702	116	45±13	2.30±0.30	split
CAN	17052140904	145	18±12	0.92±0.31	split
CAN	17165072905	94	34±8	1.17±0.23	split
CAN	13268164243	133	52	n/a	null
CAN	15315015438	144	76±13	2.04±0.10	split
CAN	16353133011	132	325	n/a	null
CAN	93192133622	143	-25±10	1.45±0.44	split
CAN	93221113831	306	-14±6	2.22±0.15	split
CAN	90290143018	149	314	n/a	null
CAN	91023011228	143	319	n/a	null
CAN	89291000414	181	281	n/a	null
CAN	97091183322	134	14	n/a	null
CAN	91292212314	123	68	n/a	null
CAN	13267112948	42	9	n/a	null
CAN	93221124247	145	60	n/a	null
CAN	93253191255	94	89	n/a	null
CAN	93225084232	122	23	n/a	null
CAN	93323014324	26	46	n/a	null
CAN	94010155350	136	314	n/a	null
CAN	94095093545	20	299	n/a	null
CAN	94119071129	150	27	n/a	null
CAN	94130063628	150	286	n/a	null
CAN	94160003160	138	33	n/a	null
CAN	94181092322	306	333	n/a	null
CAN	97023021519	145	322	n/a	null
CAN	97091183332	139	326	n/a	null
CAN	99340231228	28	11	n/a	null
CAN	07318154549	144	57	n/a	null
CAN	04320090655	121	331	n/a	null
CAN	97301062019	128	45	n/a	null

Table S3. Splitting measurements for stations TAU, MOO (Permanent stations)

Station	Event	Back-azimuth (°)	Fast-direction (°)	Splitting time (s)	Result type
TAU	00114093223	153	335	n/a	null
TAU	00133184815	148	76	n/a	null
TAU	00217211803	357	-74±11	2.07±0.43	split
TAU	01026032140	296	-57±5	1.32±0.16	split
TAU	00285201409	135	81	n/a	null
TAU	03022021135	88	339	n/a	null
TAU	03174121730	18	10	n/a	null
TAU	05080122853	151	316	n/a	null
TAU	05269020037	129	342	n/a	null
TAU	05281035535	306	-41±10	2.05±0.28	split
TAU	05321193154	146	88±18	1.15±0.35	split
TAU	06120192215	145	-44±13	1.22±0.21	split
TAU	06237004946	148	270	n/a	null
TAU	06317013136	152	72	n/a	null
TAU	07017232350	278	87±12	1.01±0.28	split
TAU	07320031800	126	-62±8	1.22±0.36	split
TAU	07353093528	20	340	n/a	null
TAU	07058211302	299	301	n/a	null
TAU	08030122109	145	-61±17	1.54±0.20	split
TAU	02091195932	147	83±13	1.65±0.28	split
TAU	08279155250	310	87±12	1.42±0.38	split
TAU	08302230958	299	-60±18	1.37±0.41	split
TAU	08303113241	297	332	n/a	null
TAU	08304151540	107	292	n/a	null
TAU	00928620215	27	280	n/a	null
TAU	11018202325	296	282	n/a	null
TAU	11341222307	146	-56±15	1.17±0.39	split
TAU	12135200039	142	-77±10	0.65±0.08	split
TAU	12176031502	9	88±7	1.62±0.15	split
TAU	13247023232	23	78	n/a	null
TAU	14057211340	23	9	n/a	null
TAU	14093024314	143	342	n/a	null
TAU	16249225403	12	64±8	1.02±0.18	split
TAU	17052140904	148	340	n/a	null
TAU	17114212830	148	342	n/a	null
TAU	99340231228	30	292	n/a	null
MOO	01145004050	1	85	n/a	null
MOO	02091195932	147	82±12	1.67±0.22	split
MOO	04320090655	121	345	n/a	null
MOO	06319111414	4	79	n/a	null
MOO	10113100306	149	77±11	1.45±0.13	split
MOO	10246111608	22	79	n/a	null
MOO	11001095658	152	358	n/a	null
MOO	11018202325 (SKKS)	296	65	n/a	null
MOO	11245134710	153	78	n/a	null
MOO	11341222307	146	-77±9	1.53±0.36	split
MOO	12080180247	94	5	n/a	null
MOO	12108035015	148	348	n/a	null
MOO	12135100039	142	271	n/a	null
MOO	12176031502	9	68±11	1.37±0.30	split
MOO	12223183742	52	50±8	1.20±0.07	split

Table S4. Splitting measurements for stationsMOO (cont'd), TOO, YNG (Permanent stations)

Station	Event	Back-azimuth (°)	Fast-direction (°)	Splitting time (s)	Result type
MOO	12149050723	26	343	n/a	null
MOO	12274163134	124	281	n/a	null
MOO	13144054449	4	13	n/a	null
MOO	13144145831	3	272	n/a	null
MOO	13274033821	3	77	n/a	null
MOO	13304230358	147	76	n/a	null
MOO	16249225403	144	58±10	1.05±0.31	split
MOO	17114213830	148	53±11	1.10±0.01	split
TOO	08187021206	4	19	n/a	null
TOO	08280083045	314	282	n/a	null
TOO	08329090300	5	13±9	1.32±0.05	split
TOO	09097042334	4	282	n/a	null
TOO	09358002333	352	3±5	2.20±0.23	split
TOO	10049011318	349	-2±9	1.75±0.37	split
TOO	10211035614	9	273	n/a	null
TOO	11246044858	184	25	n/a	null
TOO	11345095456	184	22	n/a	null
TOO	14282021431	123	-3±8	2.50±0.30	split
TOO	15269025118	148	-20±7	2.22±0.26	split
TOO	15299090942	307	38±6	1.73±0.11	split
TOO	16030032510	8	20	n/a	null
TOO	16041003305	148	26±5	2.40±0.32	split
TOO	16101102858	308	281	n/a	null
TOO	16178111711	311	23	n/a	null
TOO	16234034523	182	284	n/a	null
TOO	17086105019	147	64±13	1.58±0.12	split
YNG	04353064619	5	17	n/a	null
YNG	00545233808	315	15±6	1.57±0.05	split
YNG	05072033120	294	283	n/a	Null
YNG	05164224433	141	78	n/a	Null
YNG	05165171016	19	3±8	1.65±0.35	Split
YNG	05269015537	124	297	n/a	Null
YNG	05281035040	306	299	n/a	Null
YNG	05288100617	4	15	n/a	Null
YNG	05321192656	143	75	n/a	Null
YNG	06002061048	181	2	n/a	Null
YNG	06053221909	24	-9±8	1.42±0.28	Split
YNG	06054040405	178	76	n/a	Null
YNG	06237004446	145	77	n/a	Null
YNG	07055023623	122	355	n/a	Null
YNG	07119124158	19	-12±5	1.32±0.14	Split
YNG	07175002518	196	79	n/a	Null
YNG	07196130801	25	-16±7	1.67±0.17	Split
YNG	07202153452	145	-28±10	1.13±0.46	Split
YNG	07304134421	20	-2±8	1.45±0.12	Split
YNG	07350080920	142	26±11	1.82±0.02	Split
YNG	08041122203	183	4	n/a	Null
YNG	08082212412	20	21	n/a	Null
YNG	08280083045	312	270	n/a	Null
YNG	09059143306	183	25±10	2.24±0.16	Split
YNG	09106145706	182	-18±14	2.05±0.48	Split

Table S5. Splitting measurements for stations YNG (cont'd), MILA (Permanent stations)

Station	Event	Back-azimuth (°)	Fast-direction (°)	Splitting time (s)	Result type
YNG	10017120001	162	6	n/a	Null
YNG	10246111608	21	11±9	2.17±0.23	Split
YNG	11326184816	142	12±5	1.31±0.12	Split
YNG	12057061719	330	33±9	1.67±0.18	Split
YNG	12108035015	146	16±15	1.40±0.37	Split
YNG	12227025938	358	-6±4	2.01±0.31	Split
YNG	13045131352	358	352	n/a	Null
YNG	14043091949	312	21±12	2.12±0.27	Split
YNG	14032035844	312	22±9	1.50±0.08	Split
YNG	14093052613	140	19±14	2.20±0.16	Split
YNG	14267112948	295	76	n/a	Null
YNG	14268164243	137	88	n/a	Null
YNG	14271073407	296	286	n/a	Null
YNG	14283091948	301	75	n/a	null
MILA	13053120158	150	13±9	1.46±0.56	split
MILA	13109030552	1	289	n/a	split
MILA	13207213300	184	13±8	1.45±0.47	split
MILA	14032035845	182	-26±15	1.72±0.66	split
MILA	13106104419	289	25	n/a	null
MILA	13144145031	1	292	n/a	null
MILA	14093015829	140	-83±19	1.95±0.48	split
MILA	13242162502	21	18	n/a	null
MILA	13258162138	22	20	n/a	null
MILA	13274033820	134	21	n/a	null
MILA	14043091948	312	23	n/a	null

Table S6. Splitting measurements for stations BA01, BA02, BA03, BA04, BA05, BA06, BA07 (Temporary stations)

Station	Event	Back-azimuth (°)	Fast-direction (°)	Splitting time (s)	Result type
BA01	11248092130 (SKKS)	43	39	n/a	null
BA01	11249114702	155	65±9	0.66±0.10	split
BA01	11346073315	359	312	n/a	null
BA01	11350105405	152	50±11	1.02±0.48	split
BA01	11351147020	146	42	n/a	null
BA01	12085203657	345	313	n/a	null
BA01	12108015003	55	57	0.68±0.05	null
BA01	12149030703	308	302	n/a	null
BA02	11261104039	312	47	n/a	null
BA02	12065054601	154	24±5	0.82±0.12	split
BA02	12227005928	360	46±5	0.74±0.13	split
BA02	11245114702	154	321	n/a	null
BA02	12085203650	150	43±8	1.01±0.27	split
BA02	12149030703	154	336	n/a	null
BA02	12155224501	115	55	n/a	null
BA03	12102204139	53	293	n/a	null
BA03	12111231909	195	50±8	1.11±0.17	split
BA03	12114204019	6	17±6	1.02+0.35	split
BA03	12072103235	1	28±6	0.83±0.01	split
BA03	12133212833	308	20	n/a	null
BA03	12155224501	116	25	n/a	null
BA03	12121053938	147	28	n/a	null
BA03	12163032858	306	22	n/a	null
BA03	12171135626 (SKKS)	15	22±9	1.20±0.31	split
BA03	12171185626	15	291	n/a	null
BA03	12176011447 (SKKS)	9	24	n/a	null
BA03	12179043054 (SKKS)	103	28	n/a	null
BA03	12194120020	307	281	n/a	null
BA03	12198010824	9	24	n/a	null
BA03	12225084702	313	291	n/a	null
BA03	12227005928	359	33	n/a	null
BA03	12240023717	105	30	n/a	null
BA04	12085203657	149	-26±9	1.03±0.34	split
BA04	12149030703	153	68±8	1.68±0.21	split
BA04	12155224501	118	334	n/a	null
BA04	12121053938	146	69	n/a	null
BA05	11261104039	146	-53±11	1.45±0.09	split
BA05	12057041708	330	43±7	2.02±0.26	split
BA05	11245085546	24	38	n/a	null
BA05	12085203657	148	307	n/a	null
BA05	12108015003	147	37	n/a	null
BA06	11193181045	107	-88±12	0.75±0.12	split
BA06	12108015003	147	-70±10	1.01±0.06	split
BA06	12149030703	152	-57±4	0.82±0.05	split
BA07	11175010924	24	339	n/a	null
BA07	11245085546	152	-48±5	1.47±0.26	split
BA07	11261104039	310	-21±5	1.32±0.19	split
BA07	12085120365	148	61±6	2.14±0.32	split
BA07	12227005928	358	61	n/a	null

Table S7. Splitting measurements for stations BA08, BA09, BA10, BA11, BA12, BA13, BA14 (Temporary stations)

Station	Event	Back-azimuth (°)	Fast-direction (°)	Splitting time (s)	Result type
BA08	11245114702	152	-66±11	0.72±0.07	split
BA08	11261104039	310	-26±9	1.25±0.40	split
BA08	12085203657	148	70±8	1.40±0.06	split
BA08	12149030703	152	-89±13	0.85±0.08	split
BA08	11175010924	24	72	n/a	null
BA08	11245085546	24	69	n/a	null
BA08	12227005928	358	346	n/a	null
BA09	11245114702	152	67±3	1.75±0.19	split
BA09	12102205506	310	-4±6	0.68±0.06	split
BA09	12057041708	330	-47±17	0.87±0.13	split
BA09	12108015003	148	70±18	1.37±0.05	split
BA09	12149030703	152	83±9	0.87±0.29	split
BA10	11245085546	26	60	n/a	null
BA10	12057041700	332	50±5	1.25±0.18	split
BA10	12102205506	90	38±6	1.43±0.08	split
BA10	11245114701	155	42±8	0.82±0.12	null
BA10	12085203657	151	332	n/a	null
BA10	12108050030	150	333	n/a	null
BA10	12108015003	156	61	n/a	null
BA11	12085203657	151	-80±11	0.64±0.19	split
BA11	12102205506	90	89±4	1.05±0.08	split
BA11	12108015003	155	89±15	0.87±0.05	split
BA12	11175010924	23	25±5	0.77±0.12	split
BA12	11245114702	150	0±5	2.40±0.13	split
BA12	11246024840	182	71±6	1.40±0.20	split
BA12	11261104039	308	20±8	0.82±0.07	split
BA12	11245085546	23	335	n/a	null
BA12	12249124205	105	89	n/a	null
BA12	13020084828	359	3	n/a	null
BA12	13072011247	7	271	n/a	null
BA12	13083021831	7	270	n/a	null
BA12	12085203657	147	-5±3	1.87±0.12	split
BA12	12108015003	146	-10±6	2.40±0.08	split
BA12	12149030703	150	-16±5	1.15±0.06	split
BA12	12222003436	80	-19±5	2.47±0.25	split
BA12	13084210201	97	10	n/a	null
BA13	12085203657	147	-47±8	1.75±0.18	split
BA13	12108015003	146	-42±5	2.45±0.14	split
BA13	12321161227 (SKKS)	4	-73±12	1.75±0.04	split
BA13	13060112032	5	-65±7	1.25±0.08	split
BA13	11236154601	129	50±11	1.75±0.08	split
BA13	11245085546	23	308	n/a	null
BA13	12022035325	183	46	n/a	null
BA13	12024143054	182	35	n/a	null
BA13	12057044178	330	30	n/a	Null
BA14	11246024843	183	22±9	2.17±0.37	split
BA14	12108015003	147	21±6	1.59±0.08	split
BA14	11245114702	151	23	n/a	null
BA14	12085203650	148	286	n/a	null

Table S8. Splitting measurements for stations BA15, BA16, BA17, BA18, BA19, BA20, BA21, BA22, BA23, BA24 (Temporary stations)

Station	Event	Back-azimuth (°)	Fast-direction (°)	Splitting time (s)	Result type
BA15	11246024843 (SKKS)	183	30±7	2.45±0.21	split
BA15	11261104039	183	-10±5	1.27±0.05	split
BA15	11175010924	24	38	n/a	null
BA15	11261104039	311	308	n/a	null
BA16	11245114702	153	53±8	1.05±0.24	split
BA16	11246024843	184	24±6	1.02±0.19	split
BA16	11261104039	311	326	n/a	null
BA16	12085203657 (SKKS)	149	324	n/a	null
BA16	12258051831	194	58	n/a	null
BA16	12270213943	21	54	n/a	null
BA16	12321161227	6	55	n/a	null
BA17	11341202250	146	59±9	1.75±0.21	split
BA17	11345075446	183	-65±10	0.92±0.12	split
BA17	12085203657	149	56±7	1.54±0.09	split
BA17	12227005935	359	49±10	0.70±0.22	split
BA17	11245114702	153	322	n/a	null
BA17	11261104039	144	57	n/a	null
BA18	11246024843	184	-30±7	2.70±0.25	split
BA18	11321045224	96	46±11	1.21±0.06	split
BA18	11341202250	149	-20±6	1.37±0.09	split
BA18	12227005935	359	24±4	1.79±0.07	split
BA19	11245114702	153	47±9	2.14±0.06	split
BA19	11246024843	184	38	n/a	null
BA19	11303182500	145	310	n/a	null
BA20	11245114702	154	-31±8	2.40±0.04	split
BA20	11246024843	185	-5±3	2.12±0.08	split
BA20	11341202250	147	-30±7	2.05±0.13	split
BA20	12227005935	0	22±6	1.40±0.03	split
BA20	12249124205	108	29±5	1.92±0.31	split
BA20	12319170201	148	41±6	1.95±0.17	split
BA21	12057041708	332	25±9	1.15±0.24	split
BA21	11207163200	79	12	n/a	null
BA21	11350105405	153	277	n/a	null
BA21	12085521828	151	14	n/a	null
BA22	11236154601	134	-66±5	1.02±0.10	split
BA22	11245114702	155	55±3	1.80±0.12	split
BA22	11326164802	147	47±5	1.57±0.31	split
BA22	11345075446	185	-10±10	1.67±0.22	split
BA22	12227005935	0	38	n/a	null
BA22	12249124205	108	307	n/a	null
BA23	11175010924	26	37	n/a	null
BA23	11178212712	153	302	n/a	null
BA23	11180033637	151	36	n/a	null
BA23	12198010825	146	307	n/a	null
BA24	11193181045	134	38	n/a	null
BA24	11204042833	155	304	n/a	null
BA24	12023140442	147	37	n/a	null
BA24	12227005935	185	305	n/a	null